

Magneto - Optical Imaging of Superconducting MgB₂ Thin Films

Stephanie Maria Hümmert

Würzburg, Bavaria, Germany

A Thesis presented to the Graduate Faculty
of the College of William and Mary in Candidacy for the Degree of
Master of Science

Department of Applied Science

The College of William and Mary
August, 2007

APPROVAL PAGE

This Thesis is submitted in partial fulfillment of
the requirements for the degree of

Master of Science



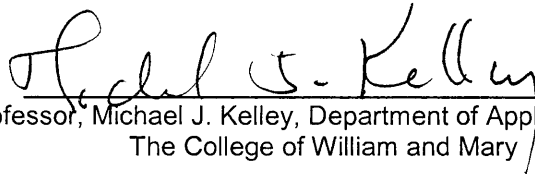
Stephanie Maria Hümmert

Approved by the Committee, July, 2007

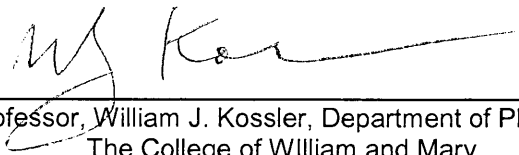


Committee Chair

Associate Professor, Gunter Lüpke, Department of Applied Science,
The College of William and Mary



Professor, Michael J. Kelley, Department of Applied Science,
The College of William and Mary



Professor, William J. Kossler, Department of Physics,
The College of William and Mary

ABSTRACT PAGE

The high-temperature superconductor MgB₂ has been studied by static and time-resolved magneto-optical imaging as a function of applied magnetic field and AC current. The averaged cross-sectional field and current profiles show a good overall agreement with the critical-state model for the field-dependent measurements. Deviations can be attributed to the irregular finger-like flux penetration typical for MgB₂. From the phase dependent measurements both shielding current and transport current profiles are obtained, which are quantitatively in good agreement with theory. The flux front growth in the MgB₂ thin film has been studied with respect to static and dynamic driving forces and analyzed in terms of the directed percolation depinning (DPD) model. The calculated exponents for static (ν) and dynamic (ν_d) measurements are in agreement with the theory. The difference in the values emphasizes the distinct effect of the driving force on the flux front growth. Based on these results MgB₂ can be placed in the same universality class as YBCO and Nb.

Acknowledgements

Thank you to everybody who contributed to the successful accomplishment of this Master thesis within one year. In particular I would like to thank:

My advisor Prof. Gunter Lüpke, who gave me the possibility to acquire this degree in his research group. Without his support this work would not have been possible.

Dr. Andrea Lucarelli for his helpful introduction to the subject, guidance and constant support. I appreciate your help and advice.

Dr. Michael J. Kelley of Applied Science and Dr. William J. Kossler of Physics for taking the time to be on my thesis committee.

Erik and Ran for proof – reading parts of the thesis.

The whole research group for the good working atmosphere.

I would also like to thank Frau Baronin von Swaine–Boist of the ‘Dr. Hildegard und Richard von Swaine-Stiftung’ who granted me a stipend allowing me to study in the USA.

Special thanks go to my mother who made all of this possible in the first place. Thank you!

Table of Contents

| | | |
|----------|--|----|
| 1 | Introduction | 02 |
| 2 | Theory | 04 |
| 2.1 | Introduction to Superconductors..... | 04 |
| 2.2 | Properties of MgB ₂ | 07 |
| 2.3 | Demagnetization Effects..... | 09 |
| 2.4 | Vortices..... | 10 |
| 2.5 | Energy Losses..... | 12 |
| 2.6 | Flux Pinning..... | 13 |
| 2.7 | Critical-State Model of C. P. Bean..... | 14 |
| 2.8 | Critical-State Model for Thin Film Geometry..... | 17 |
| 2.9 | Thermo – Magnetic Instabilities..... | 23 |
| 2.10 | Self Organized Criticality..... | 29 |
| 3 | Magneto-Optical Imaging | 33 |
| 3.1 | Faraday Effect..... | 33 |
| 3.2 | Experimental Setup..... | 36 |
| 3.3 | Calibration | 40 |
| 3.4 | Sample Characteristics | 42 |
| 4 | Analysis and Discussion | 45 |
| 4.1 | Averaged Flux Profile Analysis | 45 |
| 4.1.1 | Field - Dependent Measurements..... | 45 |
| 4.1.2 | Current Dependent Measurements..... | 54 |
| 4.1.3 | Phase Dependent Measurements..... | 58 |
| 4.1.4 | Transport Current Analysis..... | 62 |
| 4.2 | Statistical Analysis..... | 66 |
| 4.2.1 | Static Measurements..... | 66 |
| 4.2.2 | Dynamic Measurements..... | 68 |
| 5 | Conclusions | 70 |
| 6 | Appendix – Interface Growth | 71 |
| 7 | References | 73 |

List of Figures

| | | |
|----------|--|----|
| Fig. 1: | Magnetization curve for type I (a) and type II (b) superconductors. | 06 |
| Fig. 2: | Phase diagram for a type II superconductor. The mixed state, or Shubnikov phase, is separating the Meißner and the normal state..... | 06 |
| Fig. 3: | Principal lattice structure of magnesium diboride, MgB ₂ [2]..... | 08 |
| Fig. 4: | Demagnetization effect in a long rod (a), a sphere (b) and a thin film with the magnetic field applied perpendicular to the film plane. In (a) demagnetization effects can be neglected, whereas in (b) and (c) they have to be taken into consideration..... | 10 |
| Fig. 5: | Flux lines penetrating a type II superconductor in the mixed state parallel to the applied magnetic field B _a . Super currents are indicated flowing around the normal conducting cores of the vortices shielding the material from the magnetic flux. | 11 |
| Fig. 6: | Inter vortex repulsion between two adjacent flux lines caused by the Lorentz force F_L | 11 |
| Fig. 7: | Sketch of the symmetry of the applied field in case of a slab superconductor with the indicated symmetry for a thin film superconductor..... | 15 |
| Fig. 8: | A magnetic field is applied perpendicular to a thin film superconductor..... | 17 |
| Fig. 9: | Current density distribution in a thin film superconductor calculated from the critical-state model for different magnetic fields B_a applied perpendicular to the film surface. | 19 |
| Fig. 10: | Flux distribution in a thin film superconductor calculated from critical current density distribution via inversion of the Biot-Savart law..... | 20 |
| Fig. 11: | Current distribution if only a transport current is applied to the thin film superconductor. | 21 |
| Fig. 12: | The plot shows the distribution of the transport current for increasing transport current given by eq. 18..... | 22 |
| Fig. 13: | The figure shows small deviations in the current and the field profiles for a thin film where a small transport current has been applied to the thin film in the y-direction. | 23 |

| | | |
|----------|--|----|
| Fig. 14: | The image acquired with the magneto-optical imaging technique shows a flux jump into the field free region of the superconducting thin film. The other structures are flux fingers penetrating the sample from the edges..... | 24 |
| Fig. 15: | The image shows a superconducting thin film on substrate. Here only the left half is shown. The grey region corresponds to the flux penetrated region. [8]..... | 26 |
| Fig. 16: | The stability diagram as calculated from the model of Denisov et al. plotted in the H-E plane. [8]..... | 28 |
| Fig. 17: | Theoretical setup for the directed percolation depinning (DPD) model. The grey cells are already wetted. Circles indicated blocked cells. A path of blocked cells is shown which prevents the interface from moving. This is happening if the probability $p > p_c$. [21] | 31 |
| Fig. 18: | The figure shows the arrangement of the ferrite -garnet based indicator on the superconducting thin film. The polarization of the linearly polarized light incident on the indicator is rotated by an angle Θ_F | 34 |
| Fig. 19: | Principal experimental setup for the time-resolved magneto-optical imaging technique. The inset in the lower right corner shows the synchronization of the AC current with the laser pulses for dynamic measurements. [28]..... | 37 |
| Fig. 20: | The spectral sensitivity has its maximum at $\lambda = 527\text{nm}$, the wavelength used in this experiments. | 39 |
| Fig. 21: | The image shows a calibration curve for the images obtained with the magneto optical imaging technique at $\sim 10\text{K}$. The exposure time was set to 0.2s. The data has been fitted with eq. 35..... | 41 |
| Fig. 22: | Image of the MgB_2 sample that was used in this study. Evident is the rough upper edge as well as damages on both edges as a result of the cutting process. The sample size is $2 \times 10 \text{ mm}^2$. Here an area of $3.4 \times 2\text{mm}^2$ is shown..... | 43 |
| Fig. 23: | Resistivity of an MgB_2 thin film of 500nm thickness on r-plane sapphire substrate. [23] | 44 |
| Fig. 24: | The three images show the flux evolution as a function of the applied field at (a) 5.95mT, (b) 14.88mT and (c) 20.83mT. The region in the middle is dark since there is no Faraday rotation due to the lack of a magnetic field. The red frame denotes the averaging area. | 45 |
| Fig. 25: | The field profiles for the field-dependent measurements are shown as a function of the half-width w . The asymmetry between the two edges is evident..... | 48 |

| | |
|--|----|
| Fig. 26: Field profiles obtained at different applied fields (a) 2.98mT, (b) 5.95mT, (c) 9.92mT and (d) 20.83mT. The profiles are fitted with eq. 14. Clearly visible is the formation of the ‘bump’ at ~ 9 mT. For lower fields the data agrees well with the critical-state model. | 49 |
| Fig. 27: The dotted lines are the fits obtained from the critical-state model. Due to the asymmetry in the images the fit underestimates the ‘bump’ on the left side, while it overestimates the data on the right side..... | 50 |
| Fig. 28: Current density distribution calculated via inversion of the Biot-Savart law from the flux distribution. The asymmetry of the field profiles is reflected in the current distribution profiles. | 51 |
| Fig. 29: The current profiles are fitted with eq. 10 from the critical-state model. Evident are the curvature on the left and the peak on the right side of the profiles..... | 52 |
| Fig. 30: The images show the effect of an increasing applied current from 0.337A (a), to 0.386A (b,) 0.423A (c), and 0.473A (d). Clearly recognizable is the relaxation of the flux into the sample and the associated intensity decrease at the edges for increasing applied currents. | 55 |
| Fig. 31: The magnetic field profiles of the zero - phase point for different applied currents are depicted. For increasing currents the peak height reduces whereas the penetration depth of the flux increases. | 56 |
| Fig. 32: The current profiles at the zero - phase point for different applied transport currents I_T are shown. With increasing transport current the plateau height is being reduced and the area where the current is flowing is getting wider..... | 56 |
| Fig. 33: Field (a) and current (b) distribution for an applied current of $I_T = 0.337$ A. The insets show out effect of the different phase point profiles for the field and current distribution respectively. | 59 |
| Fig. 34: The left and right panel shows the flux distribution for a transport current $I_T = 0.337$ A and $I_T = 0.473$ A, respectively. Dotted lines are fits eq. 14. The dark circles mark deviations. | 60 |
| Fig. 35: The left and right panel shows the current profiles for a transport current of 0.337A and 0.473A respectively. The dotted lines are the critical-state model fits, eq. 10. | 61 |

Fig. 36: The graphs show the transport current profiles for different applied currents 0.337A (a), 0.386A (b), 0.423A (c) and 0.473A (d). The red and the blue curves represent the transport current obtained by subtracting the zero - phase point from the min. and max. phase point of the total current profiles, respectively. The data was fitted with eq. 18. Fits are represented by the dotted lines.....62

Fig. 37: The red and blue curves represent the transport current profiles obtained by subtracting the zero - phase point of the total current density of the min. and the max phase point, respectively. Comparing the total current density, dominated by the shielding current, with the transport current density one notices that the fanning out effect is occurring distinctly where the transport current is flowing. The grey area indicates where 90% of the applied current is flowing in the sample. For the higher transport current (b) the peak of the transport current profiles increases in height with respect to the lower current (a). The total current density in (a) has been rescaled by a factor of 0.5 for better comparison.65

Fig. 38: The interface from which $C(l)$ was calculated (a) and the associated double logarithmic plot of $C(l)$ over l (b) are shown. The black line indicates the value l_{sat} at which the function goes into saturation. The function was fitted with the power law eq. 40. The data was extracted from the flux front of the upper edge at an external applied magnetic field of 20.83mT. The purple line is the fit with eq. 40.67

Fig. 39: Double logarithmic plot of $C(l)$ over l . The data was extracted form the zero phase point image with a transport current of 0.423A and fitted with eq. 40 The graph shows the same distinct behavior as for the field-dependent measurements. The fit is purple, while the data points are blue.....69

Fig. 40: (a) Upper edge of the original image for an applied field of 20.83mT with contour plot corresponding to a magnetic field value of ~ 7 mT. (b) Result after averaging and excluding irrelevant data.71

Fig. 41: Expected plot for the two point correlation function $C(l)$ as a function of l for a self affine interface. [21]72

Table 1: The table shows the values for the dissipated power, the generated heat and the increase in temperature.58

Table 2: Comparison of the transport current values calculated via integration of the transport current profiles and via fitting of the transport current profiles.64

Magneto – Optical Imaging of
Superconducting MgB₂ Thin Films

1 Introduction

High-temperature superconductors (HTSC) offer a wide range of applications including particle accelerators, energy storage and alternating current systems such as electro motors and transformers. They allow both a reduction of volume, size, weight and costs of such machines, and simultaneously increase their efficiency. [1] The use in commercial power projects such as the power grid holds the prospect of lossless energy transport. However, there are problems to overcome: HTSCs can not yet fulfill the requirements for stability and low energy losses in AC systems where magnetic fields are applied perpendicular to current carrying superconducting components. [1]

In 2001 magnesium diboride, MgB_2 , a compound known since the 1950s, was discovered to be a high-temperature superconductor. Its transition temperature of $T_c = 39\text{K}$ is the highest for inter-metallic compounds so far. [2, 3] In contrast to other HTSCs, such as $\text{YBa}_2\text{Cu}_3\text{O}_{7-\delta}$ or Nb, MgB_2 faces the problem of more pronounced instabilities in the flux penetration process, which endanger electronic devices and lead to dissipation of energy. [1] Hence commercial applications are hindered by this complex flux motion. [4]

Instabilities in MgB_2 appear as finger-like structures, flux jumps or dendritic patterns, which penetrate the material within nanoseconds. [1] To describe and understand instabilities such as the finger-like penetration structure or flux jumps and dendritic patterns in MgB_2 , different models have been established. [5, 6, 7, 8, 9] Their approach focuses on the thermal properties of HTSCs such as specific heat, thermal conductivity and heat transfer instead of intrinsic properties. [7, 8] Simulations confirm the experimental findings that instabilities occur only above a certain threshold field H_{th}

[10] and beneath a threshold temperature T_{th} . [7] To successfully realize commercial application of MgB₂ in any device used in AC systems, instabilities and the associated energy losses must be analyzed and understood.

The objectives of this thesis are as follows:

- Compare the flux development in MgB₂ to the predictions of the critical-state model and recently measured data of YBCO to determine if the flux evolution in MgB₂ can be understood in terms of the critical-state model despite the typical instabilities.
- Study the effect of an AC current as a driving force behind the flux motion, and the spatial distribution of the transport current.
- Analyze the influence of static and dynamic driving forces on the flux front growth.

The thesis has the following structure: In section 2 the basic principles of high-temperature superconductors are discussed with respect to MgB₂. Afterwards the critical-state model, on which the analysis of the flux and current distribution in HTSC thin films is based, is presented along with a short introduction to self organized critical systems. The experimental setup employed to realize time-resolved magneto-optical imaging is presented in section 3. Results on the field, current and phase dependent measurements of the flux distribution are discussed in section 4 along with the findings for the static and dynamic fractal interface growth in MgB₂. A summary of the most important conclusions can be found in section 5.

2 Theory

2.1 Introduction to Superconductors

Superconductivity was first discovered by Heike Kammerlingh Onnes in 1911 when he reported the sudden loss of electrical resistance in Mercury beneath a temperature of about 4.2K. Since then various elements, compounds and ceramics have been discovered to display superconducting properties.

There are two types of superconductors. Both are characterized by the sudden loss of electrical resistance beneath a material dependent critical temperature T_c . Elementary superconductors such as Pb, Al or Hg are type I superconductors with transition temperatures lower than 7.2K, while for type II superconductors higher critical temperatures up to $\sim 135\text{K}$ can be achieved. Type I superconductors display perfect diamagnetic properties, which lead to a complete extrusion of an applied magnetic field from the inside of the superconducting material. This effect is called Meißner-Ochsenfeld effect and can not merely be explained by zero resistivity. The magnetization $M = -H$ for $T < T_c$ is the reason behind this effect. Type II superconductors, such as YBCO, Nb or MgB_2 , show a more complicated response to an applied magnetic field. Hence superconductors are classified according to their distinct behavior in an external magnetic field. The specific properties of both types are explained in more detail below.

The BCS theory introduced by and named after J. Bardeen, L. N. Cooper and J. R. Schrieffer describes the behavior of conventional superconductors. Electrons in superconducting materials are correlated via phonons and form a so called Cooper pair with another electron of opposite spin and momentum. The energy difference between normal electrons and Cooper pairs is referred to as energy gap. Cooper pairs are bosons.

This allows them to condensate into the same ground state hence reducing the energy of the system. To break up a Cooper pair the magnitude of the energy absorbed by the correlated electrons has to be greater than their binding energy. The energy required to destroy superconductivity can be provided in form of an applied magnetic field or simply heat.

Type I superconductors

The property characterizing type I superconductors is the perfect diamagnetism in an external magnetic field described by the Meißner-Ochsenfeld effect. From zero resistivity, $\rho = 0$, the material is expected to behave like an ideal diamagnet with a magnetic susceptibility $\chi = -1$. According to Lenz's law a shielding current is induced in the superconducting sample when it is exposed to an external magnetic field H_a . The supercurrent is flowing within the London penetration depth λ_L on the surface of the sample creating a magnetization $M = -H_a$. Due to zero resistivity the currents aren't minimized by electrical resistance and the induced field compensates the applied field H_a shielding the sample. However, superconductivity can be annihilated if the external magnetic field reaches a critical value H_c , which depends on both the material and the temperature. In that case a sudden transition from the superconducting state into the normal state occurs if demagnetization effects can be neglected (see figure 4).

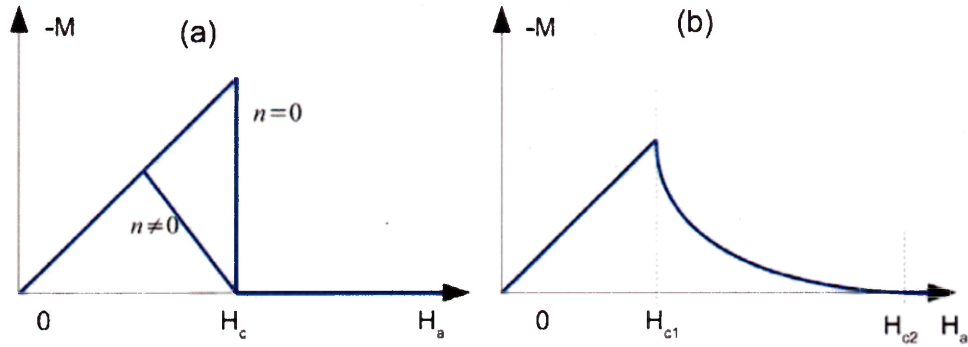


Fig. 1: Magnetization curve for type I (a) and type II (b) superconductors.

Type II superconductors

Type II superconductors have two critical magnetic fields, H_{c1} and H_{c2} . Depending on the magnitude of the applied field the superconductor is either in the mixed state or the Meißner state as depicted in figure 2.

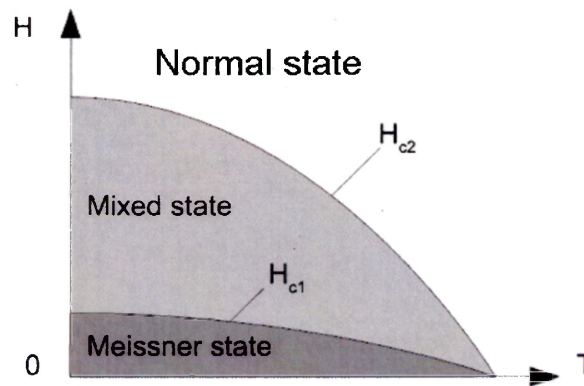


Fig. 2: Phase diagram for a type II superconductor. The mixed state, or Shubnikov phase, is separating the Meißner and the normal state.

For an applied field lower than the critical field H_{c1} the material is in the Meißner state displaying the same properties as a type I superconductor. When the applied field is higher than the upper critical field H_{c2} , the material is in the normal state and the

magnetic field penetrates the whole sample. If, however, the magnitude of the applied field is ranging between H_{c1} and H_{c2} the material is in the mixed state where quantized flux lines can partially penetrate the sample. Each flux line carries one flux quantum $h/2e$ and gradually reduces the magnetization M in the sample as shown in figure 1. The quantity and penetration depth of the flux lines is proportional to the magnitude of the external magnetic field. Despite the partial flux penetration the material is still superconducting. Both critical fields, H_{c1} and H_{c2} , are material and temperature dependent as seen in figure 2. Additionally, due to their high transition temperature they also generally possess high upper critical field values.

The fact that the energy required to destroy superconductivity can also be provided in form of a magnetic field explains why only a certain critical current can be carried by a superconductor depending on material, temperature and applied magnetic field. If a transport current is flowing in the superconducting material it induces a self field in the sample in order to shield the magnetic field of the applied current. If the field exceeds the critical magnetic field superconductivity is annihilated. The parameter used to characterize this property is the critical current density $J_c = [A/m^2]$, which is independent of the sample geometry.

2.2 Properties of MgB₂

High-temperature superconductors are type II superconductors, among them magnesium diboride, MgB₂, which has been known since the 1950s, but has just recently been discovered by the group of Nagamatsu et al. [2] in 2001 to be a high-temperature superconductor. Its transition temperature of $\sim 39K$ is the highest T_c for a binary inter-

metallic compound so far. [11] The molecular structure of this relatively simple and cheap compound is shown in figure 3. [2] Both Boron and Magnesium atoms are arranged in alternating hexagonal layers along the c-axis of the crystal with the lattice constants $a = 3.086\text{\AA}$ and $c = 3.524\text{\AA}$. [11] MgB_2 is highly hygroscopic and degrades fast in water [12] so it has to be kept in a dry environment.

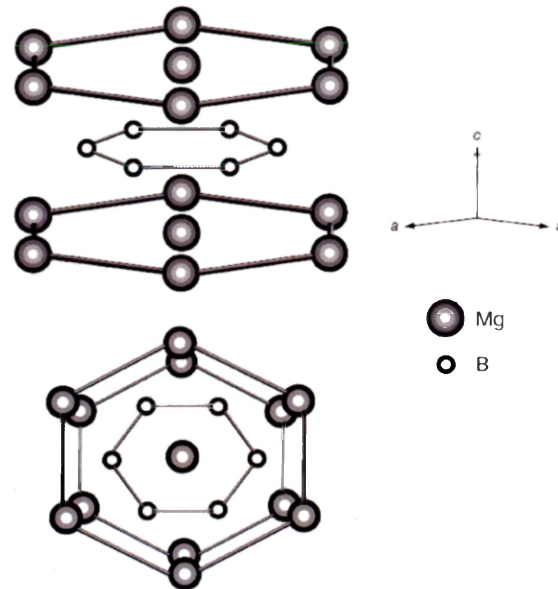


Fig. 3: Principal lattice structure of magnesium diboride, MgB_2 [2]

The correlation of electrons in MgB_2 was verified to be phonon mediated by the isotope effect, which is a fundamental test to study superconducting mechanisms. [11, 13] MgB_2 consists of light mass elements, which results in high phonon frequencies. This may be a reason for the surprisingly high transition temperature, that can not entirely be explained by the BCS theory.

Measurements of the specific heat and the isotope effect have shown that MgB_2 is a two gap superconductor. [11] This finding is in opposition to conventional behavior and is crucial to understanding the mechanisms responsible for superconductivity in MgB_2 .

[14] The superconducting energy gap is related to the formation of the Cooper pairs which are responsible for carrying charge in the superconducting state. [3] The formation of the two energy gaps was found to be related to the σ - and π - orbitals of MgB₂. According to ref. [14] the σ bands are coupled strongly to the phonons confined within the hexagonal boron layer, whereas the π bands show only very weak electron - phonon coupling. This favors the formation of Cooper pairs generating a large gap at $\sim 6 - 7\text{meV}$. The π bonding is oriented normal to the boron planes and does not couple strongly to those phonon modes, thus causing a smaller energy gap at $\sim 1 - 2\text{meV}$.

Due to the layered honeycomb structure, depicted in figure 3, the upper critical field of MgB₂ is anisotropic. At $T = 0\text{K}$ the value for $H_{c2} \sim 3 - 4\text{T}$ in a direction parallel to the c-plane and $H_{c2} \sim 15 - 20\text{T}$ normal to the c-plane. [11] This information gives some insight into why MgB₂ is interesting from a scientific point of view. Despite its relatively low T_c compared to high T_c - cuprate - superconductors it has several advantages making it attractive for electronic applications such as in Josephson junctions. MgB₂ has less anisotropy and fewer interface problems, which high T_c - cuprates are facing. [11]

2.3 Demagnetization Effects

Depending on the orientation of a superconducting sample in an applied magnetic field demagnetization effects occur due to the bending of the flux lines around the superconductor. This is because the flux lines cannot penetrate the superconductor in the Meißner state.

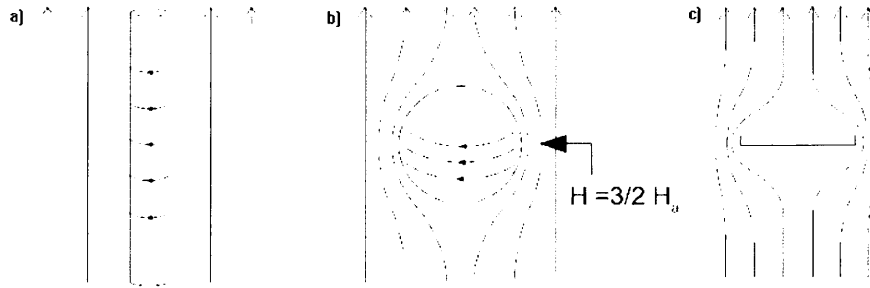


Fig. 4: Demagnetization effect in a long rod (a), a sphere (b) and a thin film with the magnetic field applied perpendicular to the film plane. In (a) demagnetization effects can be neglected, whereas in (b) and (c) they have to be taken into consideration.

In an infinitely long rod placed parallel to a homogeneous external magnetic field, demagnetization effects can essentially be neglected except at the end of the rod as depicted in figure 4 (a). In case of a sphere, see figure 4 (b), the bending of the flux lines becomes more pronounced and at its equator the magnetic field is increased by a factor of $3/2$ above the actual applied field H_a . In our case, where a magnetic field is applied perpendicular to the surface of a superconducting thin film, demagnetization effects can not be neglected as shown in figure 4 (c). The flux lines are bending around the edges of the sample, increasing the field locally. Thus penetration would start at the edges as soon as the field magnitude exceeds the critical field value H_c of the material in case of a type I superconductor.

2.4 Vortices

When a type II superconductor is in the mixed state, i. e. the external applied field ranges between H_{c1} and H_{c2} , magnetic flux lines start penetrating the sample from the edges. Flux lines penetrating a superconducting material are shown in figure 5.

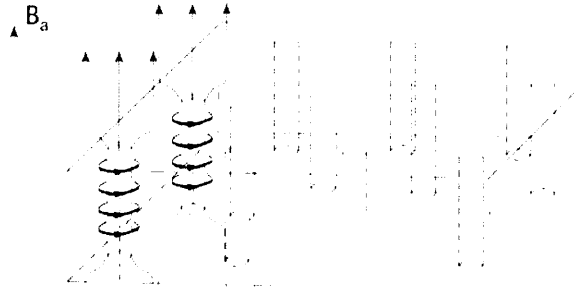


Fig. 5: Flux lines penetrating a type II superconductor in the mixed state parallel to the applied magnetic field B_a . Super currents are indicated flowing around the normal conducting cores of the vortices shielding the material from the magnetic flux.

The core of such flux lines, or vortices, is normal conducting with a radius ξ called coherence length. Each flux line is surrounded by small super currents (see figure 5) which decay over the London penetration depth λ_L , as does the magnetic field of the flux line. The total flux carried by each vortex is $\Phi_0 = h/2e$, where $2e$ relates to the charge of the Cooper pairs and h is Planck's constant.

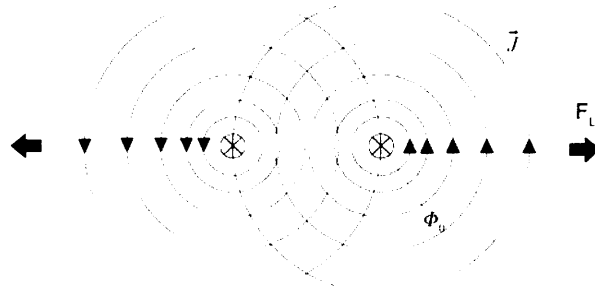


Fig. 6: Inter vortex repulsion between two adjacent flux lines caused by the Lorentz force F_L .

Inter vortex repulsion between flux lines and the shielding current of an adjacent vortex, as depicted in figure 6, is caused by the Lorentz force given by

$$\vec{F} = \vec{J} \times \vec{\phi}_o \quad (1)$$

In eq. 1 F is the Lorentz force per unit length and J is the shielding current density at the position of an adjacent vortex. This leads to the arrangement of flux lines in a regular hexagonal lattice called Abrikosov lattice. Such a regular arrangement is only possible if there are no defects or pinning sites present in the material. The case for pinning sites present in the material is discussed later.

If a transport current is applied to the type II superconductor in the mixed state the magnetic flux lines also feel a Lorentz force

$$\vec{F}(\vec{r}) = \vec{J}(\vec{r}) \times \vec{B}(\vec{r}). \quad (2)$$

F is the Lorentz force per unit volume, J the applied transport current density and B the average magnetic field of a distribution of several flux lines in the sample. The Lorentz force thus leads to a vortex movement normal to the direction of the transport current, which results in work, a drop of voltage, electrical resistance and therefore energy losses.

2.5 Energy Losses

Since the core of a flux line is normal conducting, the associated phase transitions of flux lines moving through the superconducting material cost energy. This energy is diverted either from an applied transport current or from the flowing supercurrents. Further energy losses are caused if non-superconducting electrons are accelerated by a local electrical field generated by the moving flux lines. The kinetic energy of such electrons is transferred to the crystal lattice in form of heat, which in turn leads to a finite resistance of the material. This is one problem high-temperature superconductors are currently facing.

2.6 Flux Pinning

In an ideal sample the transport current causes flux lines to permanently enter the sample on one side and exit it on the other. Since there are always defects present in real crystals acting as pinning centers, the penetration of the vortices is restrained. Pinning sites are locations in the material that stay normal conducting even below T_c , which makes them act as potential wells for flux lines. Phase transitions associated with the vortex movement through the superconductor cost energy. By passing through a normal conducting pinning site no expenditure of energy is needed to break up the Cooper pairs, as the site is normal conducting already. Hence vortices prefer passing through such pinning sites and can be ‘trapped’, held in place by the pinning force F_p .

The flux distribution reaches a non equilibrium state when the driving force of the vortices, the Lorentz force F_L , is equal in magnitude to the pinning force F_p that holds the flux lines in place. For the flux line to resume moving further into the sample the magnitude of the Lorentz force F_L and the repulsive forces between the single flux lines have to be bigger than the maximum pinning force F_p , which can be achieved by increasing the applied magnetic field. Consequently a density gradient of the penetrating vortices is generated. From eq. 2 the associated critical current density J_c , at which the vortices are being removed from a pinning site, can be obtained:

$$J_c(\vec{r}, \vec{B}) = \frac{F_p(\vec{r})}{|B(\vec{r})|} \quad (3)$$

Note that the equation contains F_p instead of F_L since the flux lines start moving again for $F_L \geq F_p$. The relation between the flux density in the sample and the corresponding supercurrents can be determined with Ampere’s law [8, 15]:

$$\nabla \times \vec{B} = \mu_0 \vec{J}(\vec{r}) \quad (4)$$

In order to analyze this relation the critical-state model has been developed, which will be introduced in the next section.

2.7 Critical - State Model of C. P Bean

Based on assumptions made by C. P. Bean [16] a model has been created capable of describing the flux and current distribution in superconducting thin films quite accurately. [17]

One of the basic assumptions of the critical-state model is that the critical current density J_c is a material dependent constant, independent of the applied and local magnetic field in the superconductor. Hence, everywhere where flux penetrates the high-temperature superconductor, the critical current density J_c is constant, as long as the applied field $B_a < B_{c2}$. This is acceptable under the condition that B_a is much lower than the upper critical field B_{c2} . The condition is fulfilled for the high-temperature superconductor MgB₂, where the value of the upper critical field B_{c2} ranges between ~15 - 20T at 0K. Hence the use of eq. 3 is justified.

The second assumption, which simplifies the matter, is that inside the superconductor $H = B$. This can be used applied the condition that the applied field is much larger than the lower critical field, $B_a \gg B_{c1}$.

The following case is applicable only for a sample that is initially in the Meißner state before the external magnetic field is increased monotonically.

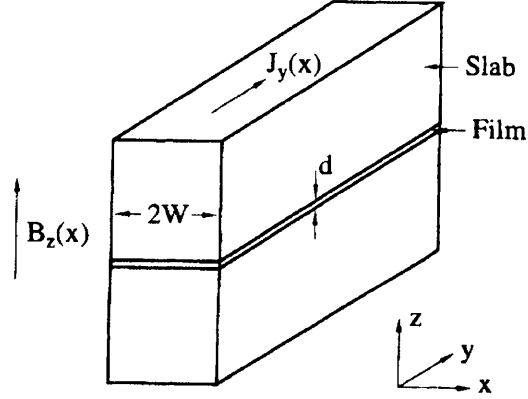


Fig. 7: Sketch of the symmetry of the applied field in case of a slab superconductor with the indicated symmetry for a thin film superconductor

A homogeneous magnetic field B_a is applied in the z -direction to a slab of width $2w$ in the x -direction, infinite length and height in the y - and z -directions, see figure 7. As in the case of an infinitely long rod, see figure 4 (a), demagnetization effects can be neglected leading to the following form of Ampere's law:

$$\frac{\partial B_z(x)}{\partial x} = -\mu_o J_y(x) \quad (5)$$

where J_y is the current density in y -direction. Here only components of the magnetic field in z -direction are considered.

If the applied field $B_a < B_{c1}$ screening currents flow at the surface of the slab within the London penetration depth λ_L , decaying exponentially towards the inside of the sample. Thus the inside of the slab is shielded from the applied field and field free. For an applied field $B_a \gg B_{c1}$ flux penetrates the slab from the edges and propagates into the sample until the pinning force F_p , corresponding to J_c , exceeds the repulsion forces between the vortices. The motion comes to a halt as soon as the current density distribution reaches

$|J(\vec{r})| \leq J_c$ as assumed by the critical-state model. Since this is the case everywhere where flux has penetrated the sample J_y in eq. 5 is replaced by J_c leading to the following current and magnetic field distribution in the slab [17]:

$$J_y(x) = \begin{cases} J_c & -w \leq |x| < -a \\ 0 & 0 \leq |x| \leq a \\ -J_c & a < |x| \leq w \end{cases} \quad (6)$$

$$B_z(x) = \begin{cases} 0 & 0 < |x| \leq a \\ \mu_o (|x| - a) J_c & a < |x| \leq w \\ B_a & |x| > w \end{cases} \quad (7)$$

where a is the half-width region in the slab where no field is penetrating, given by:

$$a = w \left(1 - \frac{B_a}{B_s} \right) \quad (8)$$

$B_s = \mu_o w J_c$ is the characteristic field at which the slab is completely penetrated by flux lines.

As long as $B_a < B_s$ there is a field free region where $B = 0$ and $J = 0$, as well as a critical region with $J = J_c$. The field free region is shielded by the screening current J_c .

The magnetic field distribution in a high-temperature superconductor depends strongly on its magnetic history. Since a certain amount of flux, which has already entered the sample, stays pinned even if the field is ramped down to zero again, a remanent state is generated.

2.8 Critical - State Model for Thin Film Geometry [17]

For thin film geometry the behavior and evolution of magnetic field and current distribution can also be modeled with the critical-state model based on the work of Bean.

There are notable differences but the basic assumptions remain:

- The critical current density J_c is a constant independent of the applied magnetic field.

This assumption is valid for superconductors with $B_a \ll B_{c2}$.

- The magnetic field inside the superconductor $H = B$, which is true if the applied field

$$B_a \gg B_{c1}.$$

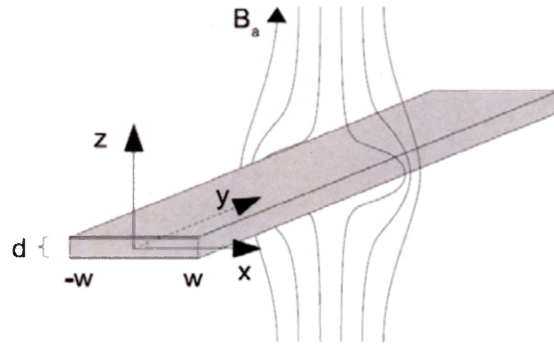


Fig. 8: A magnetic field is applied perpendicular to a thin film superconductor

As shown in figure 8, a magnetic field B_a is applied perpendicular to the surface of a type II superconducting thin film with thickness d in the z -direction and half-width w in the x -direction. The condition $\lambda_L \ll d \ll w$ applies, where λ_L is the London penetration depth for a Meißner screening current. Assuming that the film thickness d is very small, the current density is one - dimensional and Ampere's law can be written as

$$\mu_0 J_y(x) = \frac{\partial B_x}{\partial z} - \frac{\partial B_z}{\partial x}. \quad (9)$$

Here demagnetization effects can not be neglected. The first term on the right hand side concerns the bending of the flux line around the sample giving rise to the tangential components of the applied field. Relative to the first term the second can be neglected since the demagnetization effects are very strong.

In the calculation of the current distribution the basic assumption is that in the region where flux has already penetrated the film, $a < x < w$, the current density is a constant, $J_y(x) = J_c$, and is independent of the magnitude of the applied field B . See figure 9. The shielding currents flowing at the edges of the sample, however, generate a non zero magnetic field in the 'field free' region, $-a \ll x \ll a$, which in turn has to be shielded by a supercurrent flowing in that region. The current density distribution for thin film geometry is obtained via conformal mapping methods, and can be found in ref. [17].

The total current density distribution in the y -direction is shown in figure 9 and is given by:

$$J_y(x) = \begin{cases} J_c & -w < x \leq -a \\ -\frac{2J_c}{\pi} \text{ArcTan} \left(\frac{x}{w} \sqrt{\frac{w^2 - a^2}{a^2 - x^2}} \right) & -a < x < a \\ -J_c & a \leq x < w \end{cases} \quad (10)$$

with the half-width free region a defined as

$$a = \frac{w}{\text{Cosh}(B_a / B_f)} \quad (11)$$

B_f is the characteristic field for thin film geometry:

$$B_f = \frac{\mu_0}{\pi} d J_c \quad (12)$$

From the current distribution, the magnetic field distribution in the thin film can be calculated via inversion of the Biot-Savart law

$$B_z(x) = B_a + \frac{\mu_0}{2\pi} \int_{-w}^w \frac{J_y(x')}{x' - x} dx', \quad (13)$$

which yields

$$B_z(x) = \begin{cases} 0 & |x| < a \\ B_f \operatorname{Ln} \left(\frac{|x| \sqrt{w^2 - a^2} + w \sqrt{x^2 - a^2}}{a \sqrt{x^2 - w^2}} \right) & |x| > a \end{cases} \quad (14)$$

In figure 9 and 10 the current density distribution and the corresponding magnetic field distribution are plotted as a response to a magnetic field applied perpendicular to the sample surface.

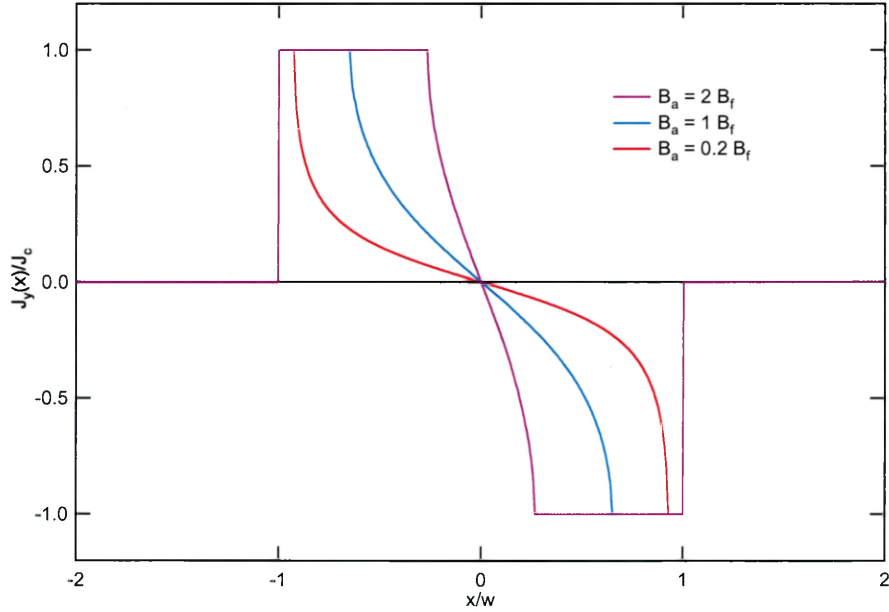


Fig. 9: Current density distribution in a thin film superconductor calculated from the critical-state model for different magnetic fields B_a applied perpendicular to the film surface.

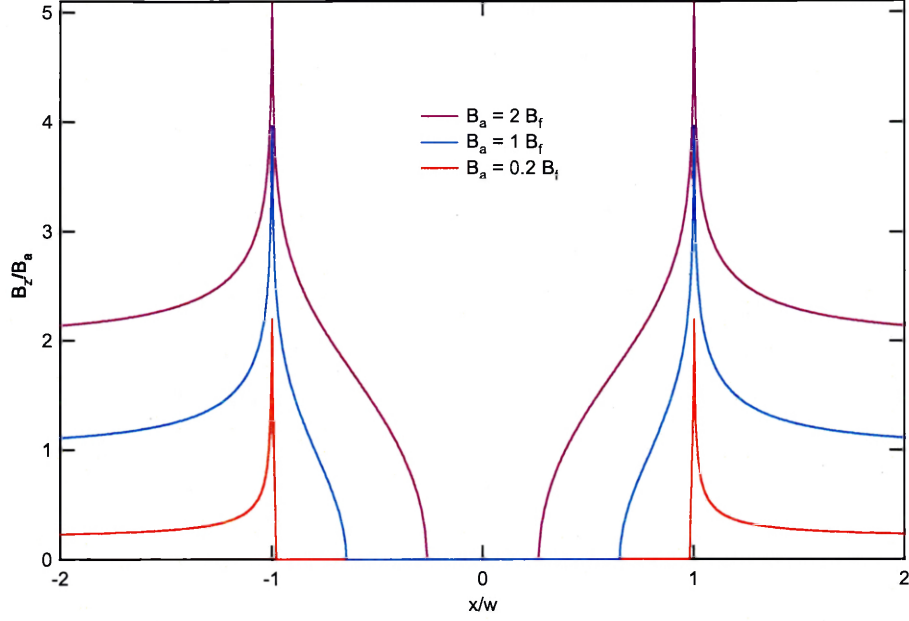


Fig. 10: Flux distribution in a thin film superconductor calculated from critical current density distribution via inversion of the Biot-Savart law.

The distribution of only a transport current applied to the superconducting thin film is shown in figure 11 and given by:

$$J_y(x) = \begin{cases} \frac{2J_c}{\pi} \text{ArcTan}\left(\sqrt{\frac{w^2 - a^2}{a^2 - x^2}}\right) & |x| < a \\ J_c & a < |x| < w \end{cases} \quad (15)$$

with

$$a = w \sqrt{1 - \left(\frac{I_T}{I_c}\right)^2}. \quad (16)$$

The corresponding field distribution is

$$B_z(x) = \begin{cases} 0 & -a \leq x \leq a \\ \pm B_f \operatorname{Ln} \left(\frac{\sqrt{w^2 - x^2}}{\sqrt{w^2 - a^2} - \sqrt{x^2 - a^2}} \right) & -a < |x| < w \\ \pm B_f \operatorname{Ln} \left(\frac{\sqrt{x^2 - w^2}}{\sqrt{x^2 - a^2} - \sqrt{w^2 - a^2}} \right) & |x| > w \end{cases} \quad (17)$$

If the magnitude of the field induced by the applied transport current reaches the value of B_{cl} at the edges of the sample, vortices start to penetrate the thin film. The penetration depth depends on the critical current density J_c of the sample.

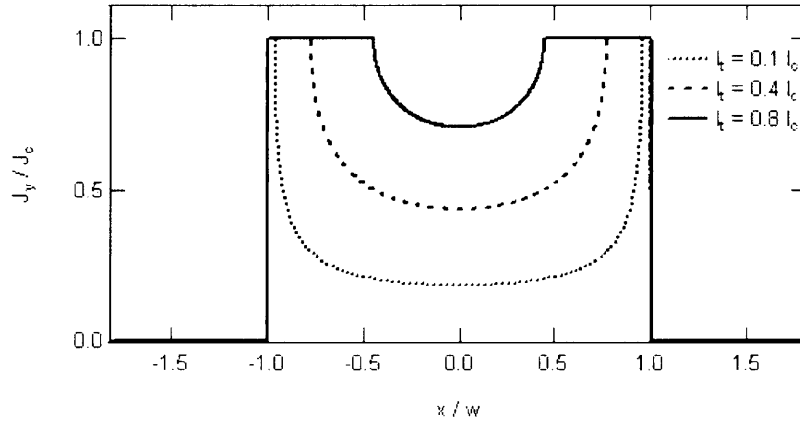


Fig. 11: Current distribution if only a transport current is applied to the thin film superconductor. [17]

In high-temperature superconductors the flux distribution depends strongly on the magnetic history of the sample due to flux pinning. Hence the above current distribution is not suitable to describe the addition of a time dependent current applied to the sample.

The current distribution of a time dependent transport current flowing in y-direction in a thin film is obtained by conformal mapping methods [17]. It is depicted in figure 12 and given by the relation:

$$I_y(x) = \frac{I_0}{\pi\sqrt{w^2 - x^2}}. \quad (18)$$

I_0 is the peak value of the applied time dependent current and w corresponds to the half-width of the thin film.

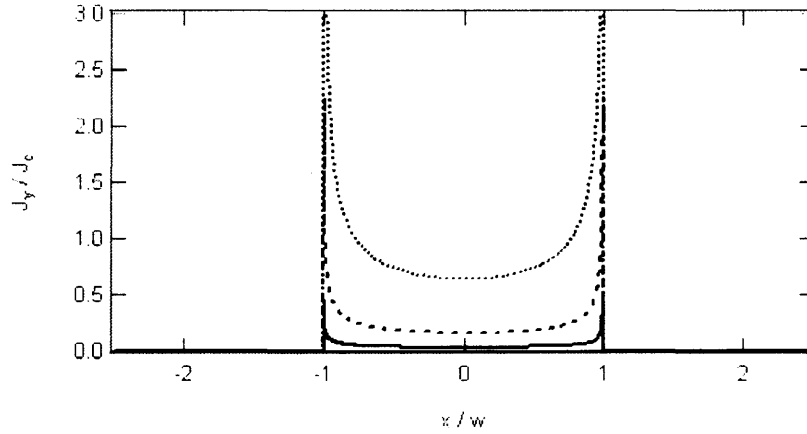


Fig. 12: The plot shows the distribution of the transport current for increasing transport current given by eq. 18

It is assumed that the transport current does not generate a field inside the strip but adds to the flowing shielding currents. Note that the singularities at the edges $\pm w$, shown in figure 12, infringe on the assumption of the critical-state model where $J(x) \leq J_c$. Nevertheless the function has been effectively used to study experimental observations before and is also successfully used to fit the transport current profiles in this study. [18]

As mentioned before the time dependent applied transport current is adding to the flowing shielding currents given in equation 10. To see the effect of a small transport current on the flux distribution an example is shown in figure 13. Here the current

distribution was re-inverted with the Biot-Savart law yielding the corresponding field distribution. The current distribution was normalized to the critical current density parameter J_c .

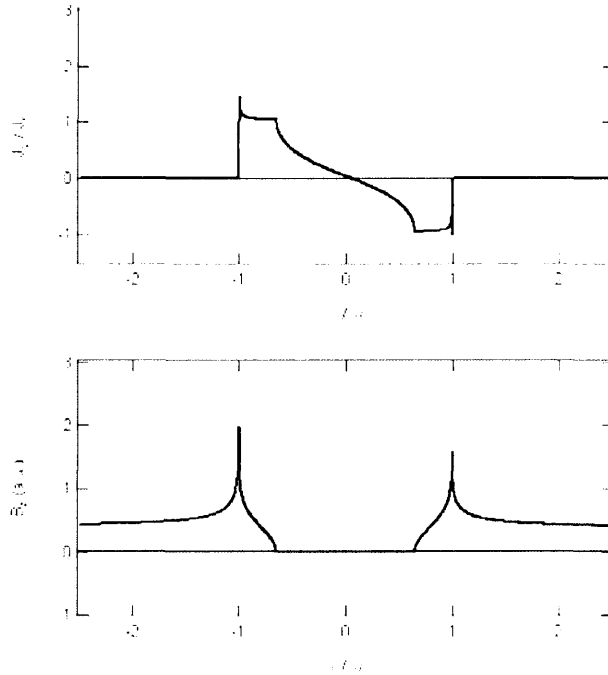


Fig. 13: The figure shows small deviations in the current and the field profiles for a thin film where a small transport current has been applied to the thin film in the y-direction.

2.9 Thermo – Magnetic Instabilities

Two basic processes in a high-temperature superconductor can evoke instabilities: (1) The flux motion initiated by ramping up the external magnetic field releases energy in form of heat and thus increases the local temperature in the superconductor; (2) Consequently the pinning force F_p is decreased by the increasing temperature, which in turn triggers further flux motion in the sample. This positive feedback loop can result in the formation of finger-like patterns and more drastic avalanches such as flux jumps or dendritic avalanches. [6] The magnetic field applied perpendicular to the sample surface

intensifies the effect. Because of the Lorentz force between single flux lines and the strong local field at the sample edge, the flux is pushed towards the centre of the thin film superconductor. This is in accordance with the observation of Barkov et al. [10] who found that dendritic avalanches usually nucleate at the edge of the sample where the local field is largest. Instabilities are generally observed in high-temperature superconductors with strong pinning at low temperatures. The phenomenon occurs very quickly, $10^4 - 10^6$ cm/s [10] and increases the amount of flux in the sample macroscopically.

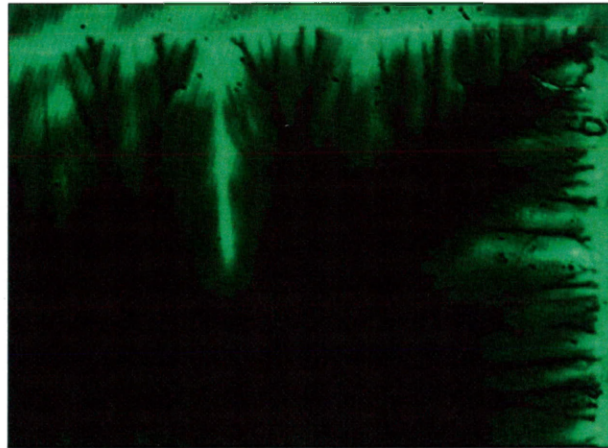


Fig. 14: The image acquired with the magneto-optical imaging technique shows a flux jump into the field free region of the superconducting thin film. The other structures are flux fingers penetrating the sample from the edges.

Figure 14 shows a flux jump observed in the sample used in this study. The finger like penetration structure resulting in an inhomogeneous flux front, however, was very evident in the acquired images, see figure 14. The growth rate of the individual fingers in MgB_2 superconducting thin films is varying, i.e. some fingers may develop faster and further into the field free region of the sample while others remain behind or are restricted in their evolution by the more developed wider flux fingers. [6] Generally the

flux fingers avoid overlapping due to long range [5, 10] repulsive forces between the vortices, creating narrow dark field free regions. For higher fields, larger fingers tend to 'swallow' smaller ones and merge together.

In order to understand the instability phenomenon more clearly, models have been established based on the Maxwell and thermal diffusion equations. Instabilities were observed only beneath a certain threshold temperature T_{th} , indicating a thermal magnetic origin. [5] The thin film is invaded perpendicular to the sample edge indicating that the Lorentz force on the vortices, created by the Meißner shielding currents flowing at the edge, is also a driving force behind those instabilities. This explains why instabilities occur preferably at concave defects at the sample edge. At such locations the screening currents are forced to flow around the defect, hence locally increasing the heat and triggering the instabilities. [10]

In the conventional linear analysis of thermo-magnetic instabilities the space time development of small perturbations in the electric field E and the temperature T are considered. Additionally non local electrodynamics and the capability of the superconductor to dissipate heat to the substrate must also be accounted for. [8]

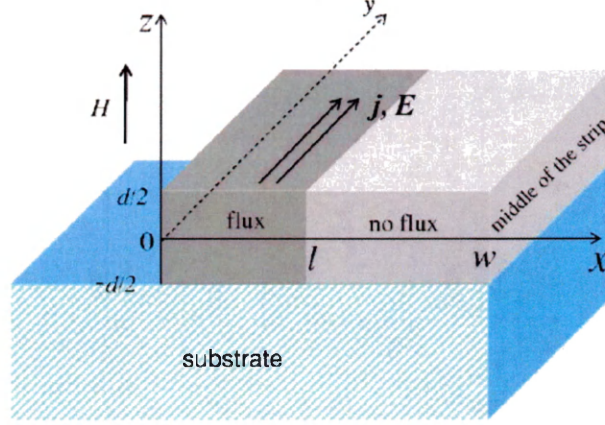


Fig. 15: The image shows a superconducting thin film on substrate. Here only the left half is shown. The grey region corresponds to the flux penetrated region. [8]

Consider the geometry shown in figure 15 where a magnetic field is applied perpendicular to a superconducting thin film with $\lambda_L \ll d \ll w$. λ_L is the London penetration depth, w the half-width of the sample and the thickness d extends from $-d/2$ to $d/2$ as indicated in figure 15. The flux distribution is calculated by eq. 5 in section 2.6 under the assumption that the critical current density J_c is independent of the applied field from Bean's model. With the help of Maxwell's induction law and the thermal diffusion equation the electric field is calculated:

$$\nabla \times \vec{E} = -\frac{\partial \vec{B}}{\partial t} \quad (19)$$

$$C \left(\frac{\partial T}{\partial t} \right) = \kappa \nabla^2 T + \vec{j} \cdot \vec{E} \quad (20)$$

C is the specific heat and κ the thermal conductivity of the material. [8] A current voltage relation of the form

$$\vec{j} = j_c(T) g(E) \left(\vec{E} / E \right) \quad (21)$$

is added to eq. 5, 19 and 20 where $g(E)$ is a non-linear function. This leads to a quasi-static critical-state with the critical current density $j \approx j_c(T)$ with j_c independent of the magnetic field B . An important dimensionless parameter in this model is τ given by:

$$\tau = \frac{\mu_0 \kappa \sigma}{C} \quad (22)$$

σ is the differential electrical conductivity. From eq. 22 the stability behavior of a thin film can already be seen. For smaller τ the heat generated by vortex motion dissipates slowly from the superconductor to the environment, leading to a local increase in temperature, that facilitates the formation of instabilities: the superconducting thin film is unstable. [8]

Equations 5, 19, 20 and 21 are solved for the case of small perturbations in the electric field E , temperature T and current density J averaged over the film thickness d and within the boundary condition given by Newton's law of cooling and Fourier's law of conduction

$$\kappa \nabla(T + \delta T) = -h_0(T + \delta T - T_0) \quad (23)$$

with T_0 being the effective environment temperature and h_0 representing the effective heat transfer coefficient.

As shown in figure 16 the appearance of the instabilities depends on the value of the heat transfer rate h_0 . The inset shows the different regions of the stability diagram.

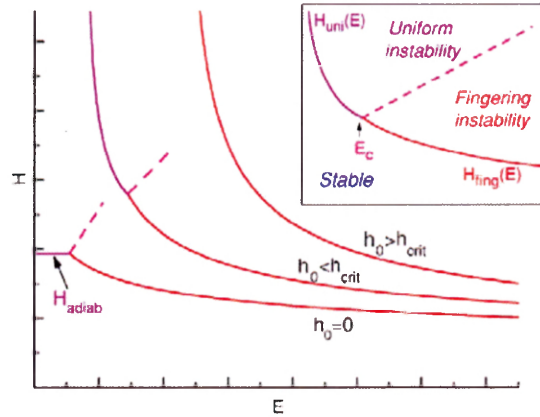


Fig. 16: The stability diagram as calculated from the model of Denisov et al. plotted in the H-E plane. [8]

As indicated in figure 16 the development of instabilities depends strongly on the electric background field E induced mainly by the applied magnetic field. For $E \gg E_c$ finger patterns are observed. The critical electric field E_c increases with the film thickness, the critical current density, the thermal conductivity and thermal coupling to the substrate. A threshold magnetic field, H_{th} , was determined to be in the order of a few mT for thin films. H_{th} as well as E_c are related to the thermal coupling parameter, h . Owing to the strong dependence of the heat capacity C and the critical current density on the local temperature, h grows swiftly with temperature indicating the existence of a threshold temperature above which instabilities are not observed. [7, 8]

Generally the onset of the finger instabilities was observed to occur after the flux had already started penetrating into the sample. The non local electrodynamics in the thin film superconductor contribute to the low magnetic threshold field for the appearance of dendritic instabilities and the low electric critical field E_c hence making thin films more unstable than bulk superconductors. A decrease in stability has been observed for thin films. [7, 8]

2.10 Self Organized Criticality

Self organized criticality describes the property of dynamic systems to “naturally evolve into a critical-state, with no characteristic time or length scales” [19] with a spatially scale invariant fractal structure. In nature many dynamical systems exist such as sand piles, bacterial growth and the spatial development of the flux front in high-temperature superconductors. In order to understand interface growth processes scaling laws are used, which are commonly accepted to study interfaces in stochastic systems. [20] Different systems can be assigned to different universality classes based upon those scaling laws and the parameter values that characterize them.

Systems, such as the motion of flux lines in a superconductor, are identified as self-affine if they are invariant under anisotropic scale transformations. Dilation of part of a self affine interface with different scaling factors for different spatial directions leads to structures similar to those observed before the rescaling. Even if not all structures can immediately be identified as similar, they usually display the same stochastic properties. I. e. the parameters characterizing the system are identical. [20, 21]

The systems are generally characterized via stochastic scaling laws. For self affine structures, such as a flux front penetrating a high-temperature superconductor, the relevant scaling relation is given by:

$$h(x) \sim b^{-\alpha} h(bx) \quad (24)$$

where the parameter α is the self-affine exponent, used to quantitatively characterize the roughness of the system. $h(x)$ is a self affine function. As mentioned before self-affine structures must be rescaled anisotropically. The factor b expands the system both

horizontally, $x \rightarrow bx$, and vertically, $h \rightarrow b^\alpha h$. The solution of above eq. 24 is a scaling law:

$$\Delta(l) \sim l^\alpha \quad (25)$$

where $\Delta(l) \equiv |h(x_1) - h(x_2)|$ is the height difference between two points separated by $l \equiv |x_1 - x_2|$. [21] In this study the spatial correlation of the flux front in MgB_2 is studied by analyzing the two point correlation function [22]

$$C(l) \equiv \sqrt{\left\langle [h(x+l) - h(x)]^2 \right\rangle_x} \quad (26)$$

which scales with the following relation:

$$C(l) \sim l^\alpha \quad (27)$$

Here the discrete directed percolation depinning model (DPD) is used to assign the system to a certain universality class.

Consider a square lattice of size l with periodic boundary conditions. Some of the cells are blocked with a probability p hindering or stopping the growth of the interface. The setup is shown in figure 17. At $t = 0$ the interface is given by a horizontal line. For every time step $\Delta t = 1$ a random unblocked cell adjacent to the current interface front is chosen and wetted as a sign of the growth process. The following conditions apply: Only cells with direct contact to the interface can be wetted, as long as it is not blocked. Simultaneously, if an unblocked cell beneath a pre-wetted one is still dry, it has to be wetted in the next time step. [21] The model is called directed percolation since the path of the wet cells is already set within certain boundaries.

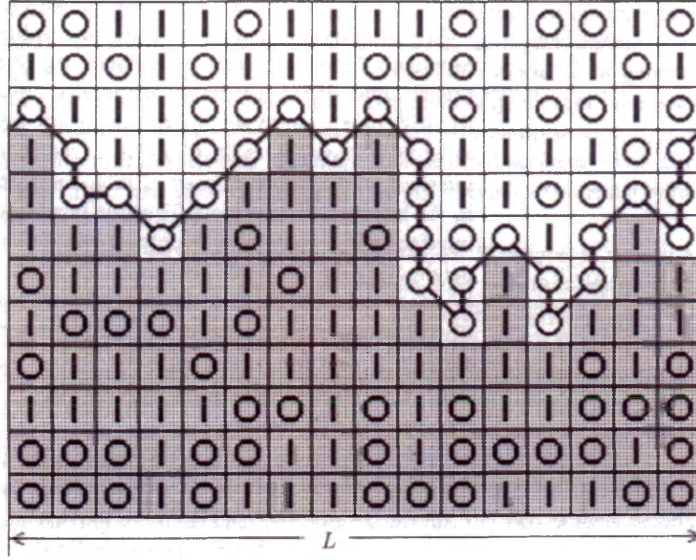


Fig. 17: Theoretical setup for the directed percolation depinning (DPD) model. The grey cells are already wetted. Circles indicated blocked cells, lines open cells. A path of blocked cells is shown which prevents the interface from moving. This is happening if the probability $p > p_c$. [21]

If the probability p lies beneath a critical probability p_c , $p \ll p_c$, the interface grows continuously. If however $p \gg p_c$ the growth stops at a certain point when it meets a ‘line’ of blocked cells spanning over the whole system size l . The blocking line is characterized by the correlation length ξ_{\parallel} parallel to the interface and ξ_{\perp} perpendicular to the interface. They are defined as

$$\xi_{\parallel} \sim |p - p_c|^{-\nu_{\parallel}} \quad \xi_{\perp} \sim |p - p_c|^{-\nu_{\perp}} \quad (28)$$

where ξ_{\parallel} gives the average length of the blocking line with the width ξ_{\perp} . The system comes to a finite halt if $\xi_{\parallel} \sim l$ with the width

$$w \sim \xi_{\perp} \sim |p - p_c|^{-\nu_{\perp}} \sim \xi_{\parallel}^{\nu_{\perp}/\nu_{\parallel}} \sim l^{\nu_{\perp}/\nu_{\parallel}} = l^{\alpha} \quad (29)$$

Since the values of the exponents $-\nu_{\parallel}$ and $-\nu_{\perp}$ are known from the model the roughness exponent can be calculated:

$$\alpha = \frac{v_{\perp}}{v_{\parallel}} = 0.633 \pm 0.001 \quad (30)$$

This model can be transferred to the problem of flux lines moving in a high-temperature superconductor. The driving force F_L corresponds to the probability $1 - p$ and the pinning force F_P to $1 - p_c$. The interface propagates into the sample at a certain speed until the pinning force holds the vortices in place bringing the system growth to a halt. This procedure occurs every time the applied magnetic field is increased. Hence the above directed percolation depinning model considers static interfaces. [20]

However, the DPD model is also valid to study the dynamical properties of moving interfaces in one - dimensional systems such as vortex penetration of a superconducting thin film. For moving interfaces the critical probability p_c is constantly altered by the driving force, which in this study is represented by an AC transport current applied to the sample. The scaling exponent is the same as in the static measurements and was numerically calculated to be $\alpha \approx 0.7$.

3 Magneto-Optical Imaging (MOI)

3.1 Faraday Effect

The basic physical principal on which the Magneto Optical Imaging technique is based is the Faraday Effect. Since the superconducting MgB₂ sample itself is not optically active, a thin film indicator is used as an optically active medium and placed directly on top of the sample.

The Faraday Effect describes the rotation of the plane of polarization of linearly polarized light passing through an optically active transparent medium when a magnetic field is applied parallel to the direction of propagation of the light. This is due to birefringence in the material causing a difference in the real index of refraction for left and right circularly polarized light proportional to the z-component of the local magnetization of the material. [15] The magnitude of the rotation angle is directly proportional to the length of the active medium which the light has to pass, as well as to the magnitude of the externally applied magnetic field.

In this study a ferrimagnetic single crystalline iron garnet thin film (Bi₃(Fe;Ga)5O₁₂) is used to analyze the flux distribution in the MgB₂ superconductor. It has an in-plane magnetization M_s that is rotated out of plane when a magnetic field is applied perpendicular to the film surface by an angle

$$\varphi = \text{ArcTan}(H_z / H_k) \quad (31)$$

where H_k represents the thin film's magnetic anisotropy field.

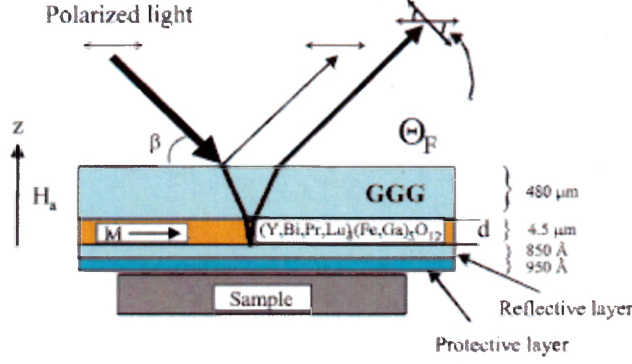


Fig. 18: The figure shows the arrangement of the ferrite -garnet based indicator on the superconducting thin film. The polarization of the linearly polarized light incident on the indicator is rotated by an angle Θ_F .

Figure 18 shows the principal structure of the indicators used here. On the Ga-Gd garnet substrate the indicator layer is grown epitaxially with a thickness of $d \sim 6\mu\text{m}$. Between the protective layer and the indicator the film also has a reflective layer of aluminum so the incident light is reflected and has to pass the indicator twice. The protective layer prevents scratching of the indicator when it is mounted on the sample. For the films the Faraday rotation is $\sim 1.08^\circ/\mu\text{m}$ for an external applied magnetic field of $H_a = 75\text{mT}$.

The linearly polarized light incidenting perpendicular to the indicator surface experiences a rotation Θ_F directly proportional to the magnetization in the z-direction M_z . Hence the Faraday rotation angle is given by:

$$\Theta_F = cM_z = cM_s \sin \varphi = cM_s \sin \left[\text{ArcTan} \left(H_z / H_k \right) \right] \quad (32)$$

where c is a material dependent constant also proportional to the path length the light has to travel in the optically active medium.

Since the indicator is placed directly on top of the superconducting thin film the spatial flux distribution in the indicator mirrors the one in the sample. The information

about the two dimensional flux distribution given in terms of an intensity distribution is resolved with a polarizing microscope and recorded with a digital camera. By inserting eq. 32 into Malus' law, $I(\alpha) = I_0 \sin^2(\alpha)$, the intensity I transmitted by two crossed polarizers, after experiencing a Faraday rotation in between the two, can be calculated:

$$I = I_0 \sin^2(\Theta_F) = I_0 \sin^2\left(cM_s \sin\left[\text{ArcTan}(H_z / H_k)\right]\right) \quad (33)$$

That is if I_0 is polarized at an angle $\pi/2 + \alpha$ relative to the polarizer. However, the extinction of crossed polarizers is not perfect. In order to make the above equation 33 more realistic a small deviation of the polarizers $\Delta\alpha$ from total extinction as well as the background intensity I' are added to the function:

$$I = I_0 \sin^2\left(cM_s \sin\left[\text{ArcTan}(H_z / H_k) + \Delta\alpha\right]\right) + I' \quad (34)$$

As mentioned before the camera records the two dimensional intensity distribution $I(x, y)$ which changes due to the magnitude of the applied magnetic field. By inverting the upper eq. the distribution of the flux can be calculated:

$$B_z(x, y) = B_k \tan\left[\frac{1}{cM_s} \text{ArcSin}\left(\sqrt{\frac{I(x, y) - I'}{I_0}} + \Delta\alpha\right)\right] \quad (35)$$

The spatial resolution depends strongly on the distance h between indicator and superconducting sample, even more than the magnification of the polarizing microscope. The smaller the distance the better the resolution and contrast. Defects, scratches or magnetic domains also contribute to a 'distorted' display of intensity. Bloch walls for example can clearly be seen in our measured images. Their intensity has been reduced by background correction but they are still clearly visible influencing the flux profile if taken into account.

3.2 Experimental Setup [28]

The MgB_2 thin film is mounted directly on top of the cold finger of the cryostat. Silver paint applied to the bottom of the sample is used to both fix it and ensure good thermal contact. Directly on top of the sample the ferrite garnet based indicator is fixed with thin strips of aluminum foil. Since the sample itself lacks proper contacting two contact pads made of tin are attached directly to the sample surface next to the indicator with insulating tape. Additionally they are held in place with a mask made of beryllium-copper, that is screwed to the cold finger, pressing the pads to the sample to enhance the contact. In the normal state the resistance was measured to be $\sim 3\text{-}4\Omega$. After zero - field cooling to $\sim 5\text{K}$ the contact resistance was at $\sim 1\Omega$.

For the magnetic field-dependent measurements a LabView program controlling the power source for the electro magnet, the camera and heating systems was used. The program increases the field linearly with a chosen step size of afore fixed values and simultaneously takes pictures with every desired step of the magnetic field. While displaying the information of the current temperature, magnetic field and current the values are stored for every step in a separate text file as well, so that they can be reviewed for significant deviations after the measurements. The program is capable of completing a field-dependent measurement within a few minutes, thus saving time and helium.

The principal experimental setup needed for the time-resolved magneto-optical imaging technique is shown in figure 19. It is composed of an optical cryostat, a solenoid electromagnet generating a magnetic field perpendicular to the sample surface, a

polarizing microscope with a CCD camera mounted on top, light sources such as a mercury lamp and laser light ($\lambda \sim 527\text{nm}$), a computer and an AC power source to apply current to the sample.

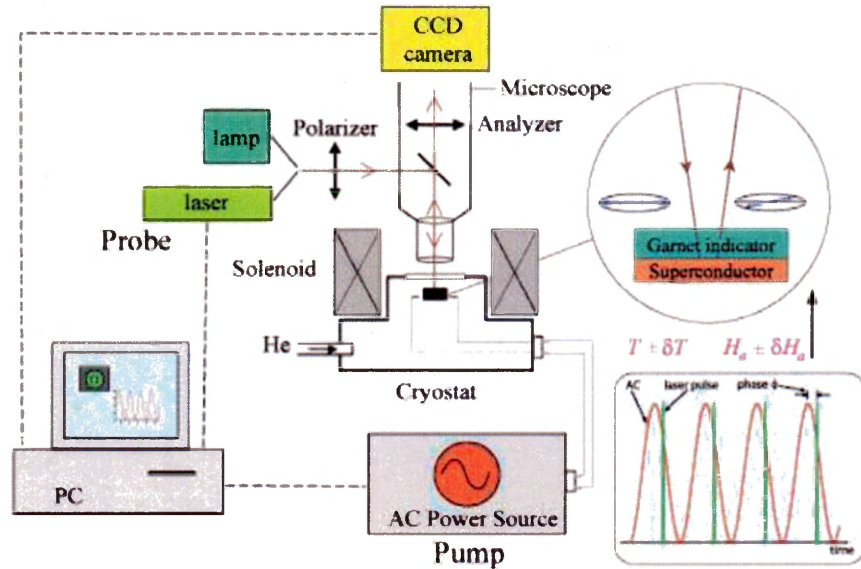


Fig. 19: Principal experimental setup for the time-resolved magneto-optical imaging technique. The inset in the lower right corner shows the synchronization of the AC current with the laser pulses for dynamic measurements.

As mentioned before the thin film is fixed on top of the cold finger of the *optical cryostat*. Temperature regulation is realized by an adjustable continuous flow of helium through the optical cryostat and a heating device attached to the cold finger to keep the set temperature stable. It is necessary to use liquid helium to cool the MgB_2 sample below its critical temperature of $T_c \sim 38\text{K}$. The cryostat's standard temperature range is 3.5K to 450K. A thermal sensor is integrated/implemented into the cold finger about 1cm beneath the sample and another is placed about 1mm beneath the top of the cold finger. To get accurate values for the applied magnetic field a Hall sensor should be attached directly beneath the sample. This however is not possible since the sample was attached directly

to the cold finger. Calibration curves were measured before the experiments for current values of 5.5A to -5.5A with the Hall sensor fixed at the later position of the sample. They show a linear correlation between current and magnetic field. The observed slight hysteresis lies within the error of the magnetic field measurement and can be neglected. Also connected to the cryostat is a pump to evacuate the optical cryostat. This is necessary to prevent condensing of water on the hygroscopic MgB₂ sample or the optical sapphire window thus preventing insight into the cryostat. The vacuum at which the measurements are conducted is $\sim 2 \cdot 10^{-5}$ Torr.

The sample is fixed in the middle of a cylindrical *electromagnet*, capable of creating a homogeneous magnetic field from - 65mT to 65mT perpendicular to the sample. The magnet is placed on top of the cryostat as shown in figure 19.

With the help of a polarizing microscope and a CCD camera the two dimensional flux distribution can be observed in real time.

The *polarizing microscope* consists of components from Olympus. It contains a Glan Thompson polarizer and linear polarizer with an extinction ratio of $\sim 10^5$. The angle between polarizer and analyzer can be adjusted easily by hand. A fluorite tension free 4x magnification objective is used, that can be replaced by a fluorite tension free 10x magnification objective for higher resolution.

The *camera* is a Hamamatsu ORCA-ER-1394 CCD camera mounted on the polarizing microscope directly on top of an adaptive optic device with a demagnification of 0:63x, to increase the field of view. The camera resolution is 1344x1024 pixels and the

exposure time can be varied from 10^{-5} to 4600s. The exposure time depends on the intensity of the laser light, which changes with the frequency of the applied current and the number of light pulses reaching the sensor per second respectively. The maximum of the camera's spectral sensitivity lies at a wavelength $\lambda = 527\text{nm}$ which is also where the wavelength of the used laser lies as shown in figure 20.

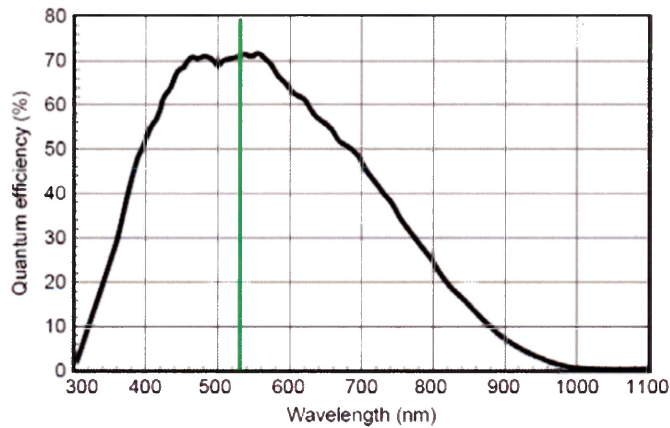


Fig. 20: The spectral sensitivity has its maximum at $\lambda = 527\text{nm}$, the wavelength used in this experiments.

The images are stored on a computer connected to the camera for later processing. It was determined via calibration that the length corresponding to one pixel is $\sim 2.5\mu\text{m}$, i.e. the total observed area of the sample is $2.56\text{mm} \times 3.35\text{mm}$. The area over which has been averaged is $2.56\text{mm} \times 1.75\text{mm}$.

Two **light sources** are available for the measurements.

A *Hg lamp* implemented in the microscope is used for static measurements only. Its advantage over the laser light is its incoherence hence generating no interference patterns that may disturb the images.

For dynamic measurements linearly polarized *laser* light with a wavelength of 527nm is decoupled from a lamp pumped Nd:YLF laser via an optical fiber and coupled

into the polarizing microscope with the help of a telescope. The telescope improves the homogeneous intensity distribution in the recorded films by expanding the light with a series of lenses. The energy output per pulse of the Nd:YLF, a neodymium-doped laser based on YLF (yttrium lithium fluoride) crystals, is $\sim 25\text{mJ}$. The 100nm short laser pulses are produced by a Pockels Cell. Repetition rates can go up to 10kHz. For our measurements however only the range between 15Hz to 1kHz was employed when triggering the laser externally for current phase dependent measurements. In order to reduce interference effects of the laser light several optical components, such as beam splitter or the optical window of the cryostat, are coated with an anti-reflection layer.

For current or phase dependent studies of the magnetic field distribution the illumination of the sample has to be synchronized with the sinusoidal AC current applied to the sample. This is accomplished by exactly synchronizing the pulse repetition frequency of the laser (external triggering) with the desired phase point of the applied AC current. Thus light reaches the camera sensor only at the chosen phase point and the image contains information about the magnetic field distribution at the desired phase point only. The exposure time of the CCD camera is longer than one period of the AC current, i. e. the obtained image contains the averaged information of the distribution over many periods and light pulses.

3.3 Calibration

To obtain quantitative results from the magneto-optical images they need to be calibrated. Hence a set of images is acquired at applied fields from 0 to about 37mT in steps of $\sim 1\text{mT}$ after zero - field cooling the sample with the indicator on top to about 5K.

For calibration the average intensity in an area far away from the sample is calculated and plotted as a function of the applied field. The area is defined as far away as possible from the sample since the influence of the sample is not desired in the calibration. With a sample width of 2mm there were only small areas undisturbed by the intensity in the sample. This calibration curve is then fitted with eq. 35 in section 3.1 to obtain the values of the various parameters, see figure 21. [15]

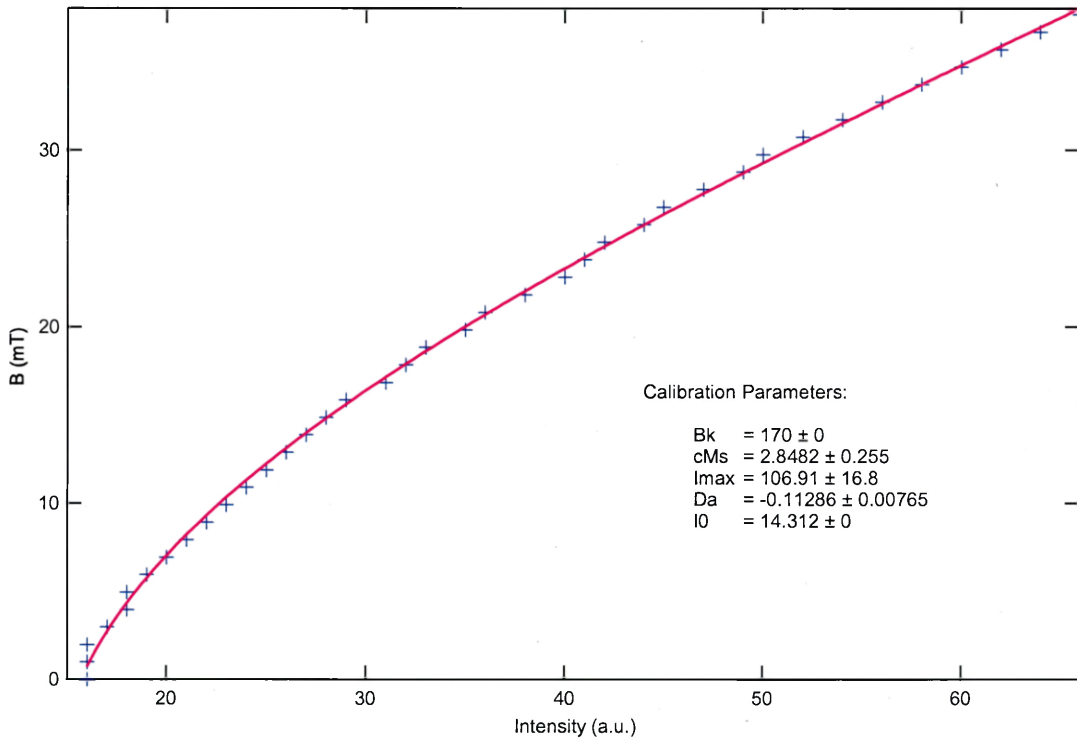


Fig. 21: The image shows a calibration curve for the images obtained with the magneto optical imaging technique at $\sim 10K$. The exposure time was set to 0.2s. The data has been fitted with eq. 35.

The calibration curve in figure 21 has been fitted with the following values:

| B_k | cM_s | I_0 | $\Delta\alpha$ | I' |
|-------|--------|--------|----------------|--------|
| 170 | 2.8482 | 106.91 | -0.11286 | 14.312 |

The intensity in the magneto-optical images depends both on the Faraday effect and exposure time and the number of laser pulses detected by the sensor in the CCD camera during that period. Such differences in images, obtained with different frequency and exposure time settings, have to be compensated before calibration. The intensity I picked up by the camera has a directly proportional relation to frequency f and exposure time τ :

$$I = f \cdot \tau \cdot \sigma + B \quad (36)$$

where σ is the intensity of on Faraday rotated laser pulse registered by the camera. B is the measured background intensity probably generated by noise in the camera. By determining B from eq. 36 the intensity in a set of images can be altered to match the conditions under which the calibration images were taken, i.e. equal number of light pulses hitting the camera sensor during the set exposure time. [29] This is possible with the following equation:

$$I_2 = \frac{f_2 \tau_2}{f_1 \tau_1} (I_1 - B) + B \quad (37)$$

3.4 Sample Characteristics

For the measurements a 2mm by 10mm sample grown by reactive evaporation with a thickness d of $\sim 500\text{nm}$ and a transition temperature of $T_c = 38 - 39\text{K}$ is used. [23] At a temperature of 36K the critical current density J_c was measured to be $\sim 10^{10}\text{A/m}^2$. [23] An image of the sample is shown in figure 22. The sample was produced by the group of Moeckly and Ruby who also developed the deposition technique. [23]

The transition between normal and superconducting state is very sharp, $\Delta T \sim 0.2\text{K}$, indicating a clean film. Despite the lattice mismatch between MgB_2 and the r-plane

sapphire substrate, the film was verified to be epitaxial and well oriented via transmission electron microscopy and electron diffraction. [23]

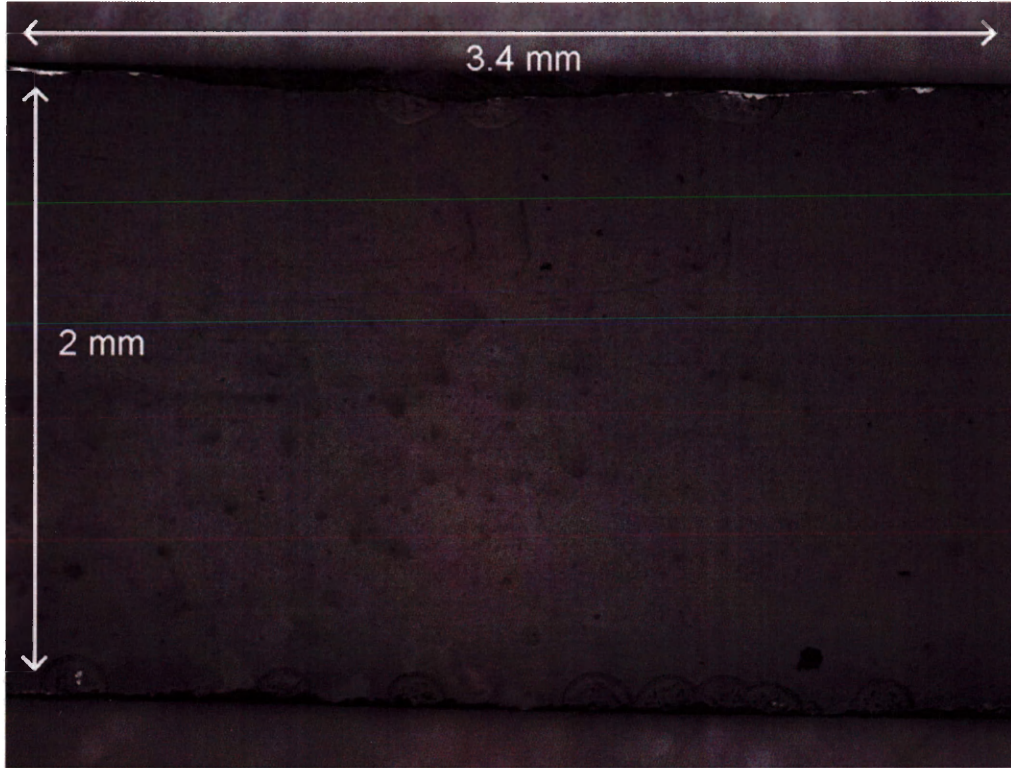


Fig. 22: Image of the MgB₂ sample that was used in this study. Evident is the rough upper edge as well as damages on both edges as a result of the cutting process. The sample size is 2 x 10 mm². Here an area of 3.4 x 2mm² is shown.

Normal state resistivity at ~ 300K was measured to be ~10μΩ cm, which approaches the best single crystal value. So does the difference resistivity between 40K and 300K of ~8μΩ cm. Figure 23 shows the residual resistivity at ~2.6μΩ cm (best single crystal value for residual resistivity ~ 1μΩ cm), presumably due to scattering at the grain boundaries of the thin film. This low value for MgB₂ indicates that the bulk of the grains are clean. The grain size lies at ~100nm.

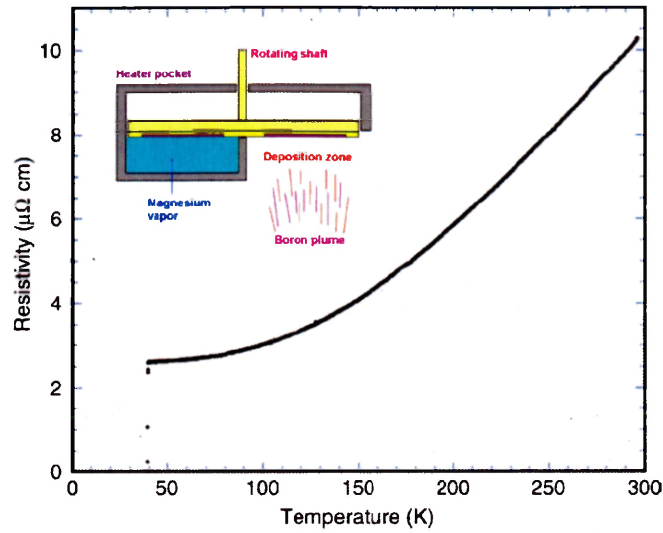


Fig. 23: Resistivity of an MgB_2 thin film of 500nm thickness on r-plane sapphire substrate. [23]

In contrast to most MgB_2 thin films this sample has a very stable thin surface layer of $\sim 2\text{-}3\text{nm}$ thickness of magnesium - and boride - oxides, preventing the decay of the material over months. Even after exposure to de-ionized water for more than $24h$ no change in the critical temperature T_c was registered and only a small rise in resistivity of $\Delta\rho \sim 2\mu$.

4 Analysis and Discussion

4.1 Averaged Flux Profile Analysis

4.1.1 Field - Dependent Measurements

The magnetic flux penetration in an MgB_2 thin film is studied as a function of an external magnetic field, applied perpendicular to the sample surface. In order to understand the behavior of the magnetic flux penetration in MgB_2 the results are compared to the critical-state model and to previously measured data on YBCO thin films.

The MgB_2 thin film is zero-field cooled to $T = 10\text{K}$. Then an external magnetic field is applied perpendicular to the surface of the thin film and ramped up from 0mT to 25mT with a fixed step size of $\sim 0.5\text{mT}$. Magneto-optical images are acquired with an exposure time of 0.2s .

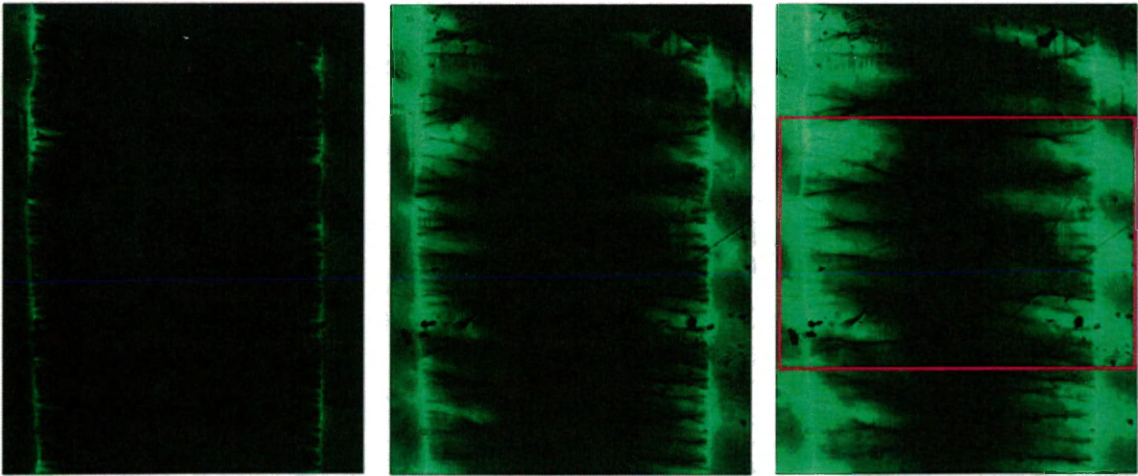


Fig. 24: The three images show the flux evolution as a function of the applied field at (a) 5.95mT , (b) 14.88mT and (c) 20.83mT . The region in the middle is dark since there is no Faraday rotation due to the lack of a magnetic field. The red frame denotes the averaging area.

Figure 24 shows the evolution of the flux as a function of the applied magnetic field. The increasing applied magnetic field affects the flux distribution in the superconducting MgB₂ sample, pushing the flux further into the sample from the edges. The dark region in the center of the sample is in a full Meißner state. The bright areas at the edges indicate the flux-penetrated region.

The flux front of MgB₂ is very irregular (figure 24) and can be best described as finger-like. It differs greatly from the smooth and homogeneous flux front generally observed in YBCO. These finger-like patterns dominate the images from the onset and grow more pronounced in both length and width as the applied magnetic field increases. They seem to avoid overlapping, which leads to the narrow flux free dark spaces between the fingers. For higher fields, however, individual fingers grow faster and hinder smaller ones in their growth.

The appearance of the finger structure is independent of the step size of the increasing magnetic field and they occur in the whole sample. Usually the fingers are expected to originate at different locations, but due to the rough edges of the sample the flux starts penetrating at mostly the same places, independent of the temperature or the step size. This is because of the strong demagnetization effects and the shielding currents flowing around the defect sites, which increase the local temperature.

At lower fields the flux front on the right side is growing faster than on the other side. The magneto-optical images show that the flux grows into the MgB₂ sample differently from the two edges. At applied fields $H_a < 10\text{mT}$ the flux front on the right edge is growing faster than on the other side. For fields $H_a > 10\text{mT}$ the left side shows a more pronounced growth of the flux as can be observed on the basis of the brighter area

on the left side of the sample. Since the brighter area is notable for every value of the applied field the behavior may be related to the rough and uneven edge close to this region. Additional flux can be admitted into the sample at these defects due to the enhanced demagnetization effects in such areas.

To gain a more quantitative understanding of the flux front evolution in MgB_2 , the averaged magnetic field cross section is studied as a function of the applied magnetic field. This approach has the advantage that signals due to smaller defects in both indicator and sample are averaged out. Furthermore, major defects can be excluded by selecting the sample area with the best signal to noise ratio that corresponds to $\sim 2.5 \times 1.8 \text{ mm}^2$. However, this analysis does not take the irregular, finger-like penetration structure of the flux into account, which is typical for MgB_2 . The images have been background corrected to enhance the signal quality and calibrated following the procedure in sect. 2.

Figure 25 shows the distribution of flux in the MgB_2 thin film across the sample width w as a function of the external magnetic field. For clarity only a few of the profiles are presented here. As predicted by the critical-state model the flux penetrates the sample from the edges where the value of the applied field is maximal. The line profiles show small wiggles that correspond to the signal of Bloch walls. They are visible as slightly brighter areas with respect to the average intensity and aligned parallel to the sample edge, hence contributing notably to the average intensity.

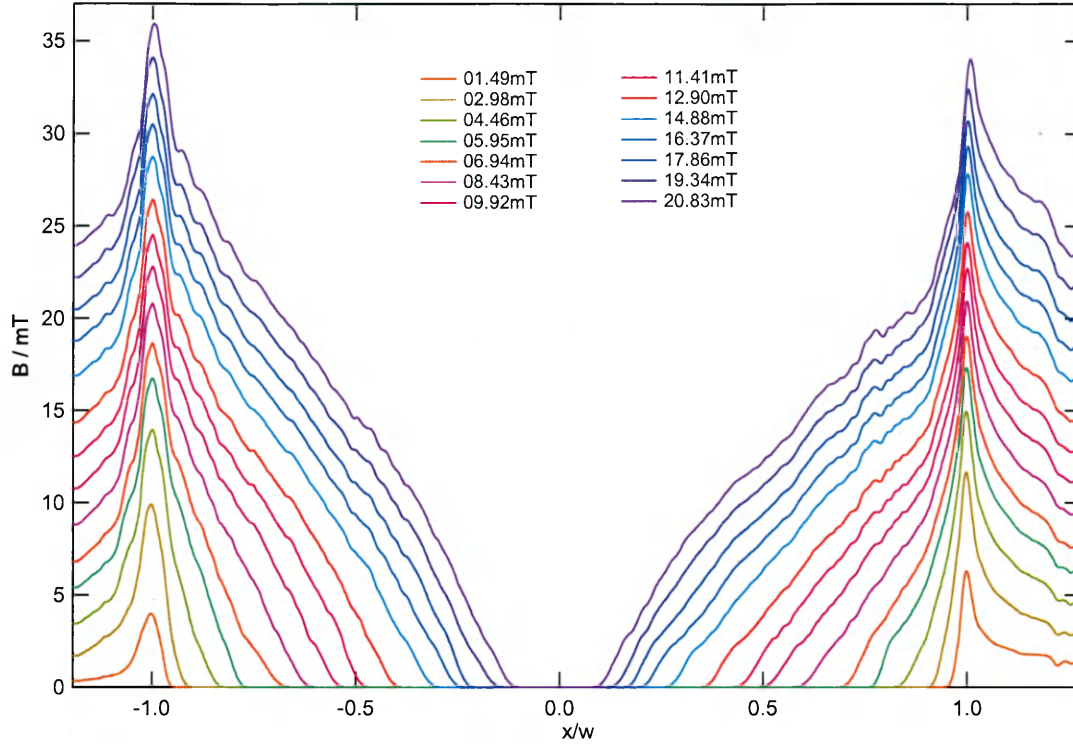


Fig. 25: The field profiles for the field-dependent measurements are shown as a function of the half-width w . The asymmetry between the two edges is evident.

The profiles in figure 25 are slightly asymmetric and show a 5 – 10% difference in peak height for different applied magnetic fields. The peak on the left is broader than the peak on the right due to the roughness on that side of the edge.

We compared the measured field profiles with the predictions of the critical-state model using eq. 14. Figure 26 shows the fits of different magnetic field line profiles for different applied fields. For magnetic field values below 6mT, the data shows a good agreement with the critical-state model.

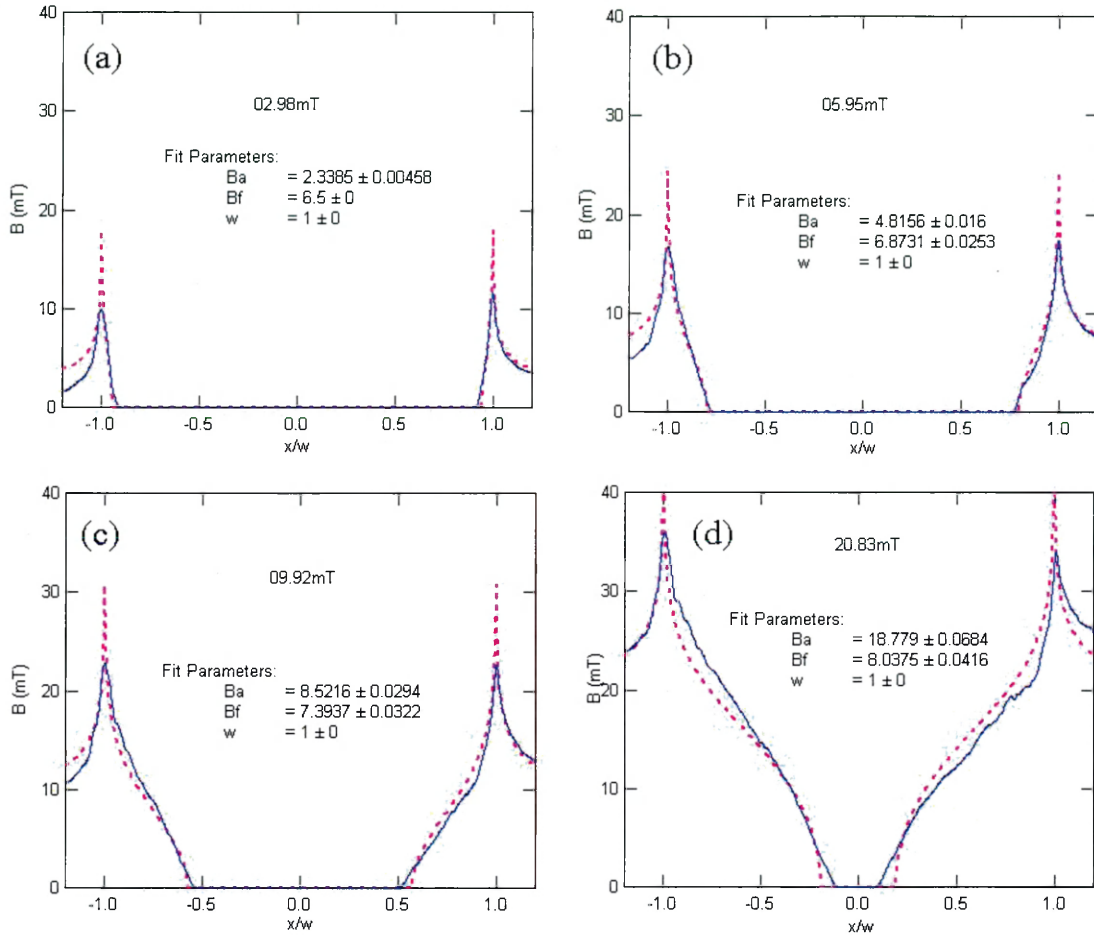


Fig. 26: Field profiles obtained at different applied fields (a) 2.98mT, (b) 5.95mT, (c) 9.92mT and (d) 20.83mT. The profiles are fitted with eq. 14. Clearly visible is the formation of the ‘bump’ at ~ 9 mT. For lower fields the data agrees well with the critical-state model.

The peak height of the magnetic field profiles at the sample edges is reduced with respect to the fits. This effect is due to the limited resolution of the measurements that results in a smoothing of the divergence expected in the ideal theoretical case.

Despite the overall good agreement of the field profiles with the critical-state model the effect of the irregular finger-like penetration of the flux in the images (figure 24) is evident. The inhomogeneous growth is reflected in the averaged profiles as a ‘bump’, which forms at the left sample edge indicated by the black arrow in figure 27. For applied fields $H_a > 9$ mT it grows more pronounced.

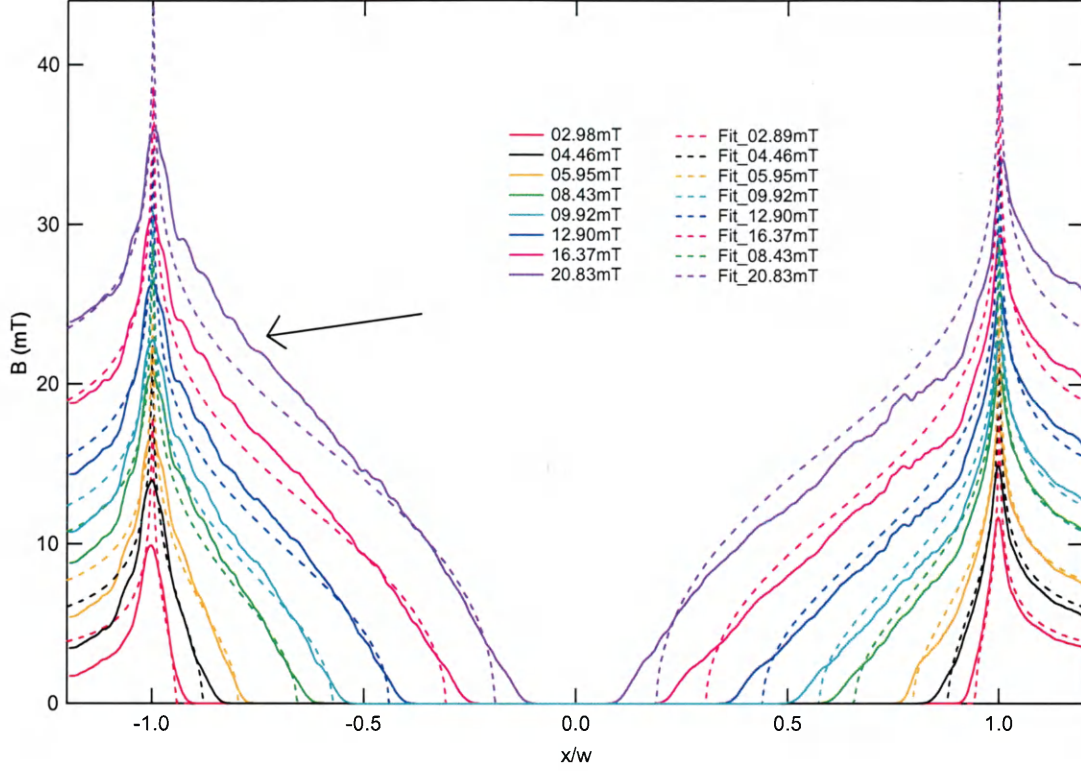


Fig. 27: The dotted lines are the fits obtained from the critical-state model. Due to the asymmetry in the images the fit underestimates the ‘bump’ on the left side, while it overestimates the data on the right side.

Figure 27 shows clearly that, due to the asymmetry of the field profiles, the fits underestimate the data on the left and overestimate it on the right side while for lower fields the agreement with the model is pretty good.

The critical current density J_c , which is proportional to the characteristic field B_f , is obtained from the fitting parameters:

$$J_c = \frac{\pi}{\mu_0 d} B_f \quad (38)$$

The critical-state model predicts a constant J_c for different applied fields, but a variation of $\sim 20\%$ was observed in J_c as the applied magnetic field was increased. This variation can be better understood analyzing the current density profiles.

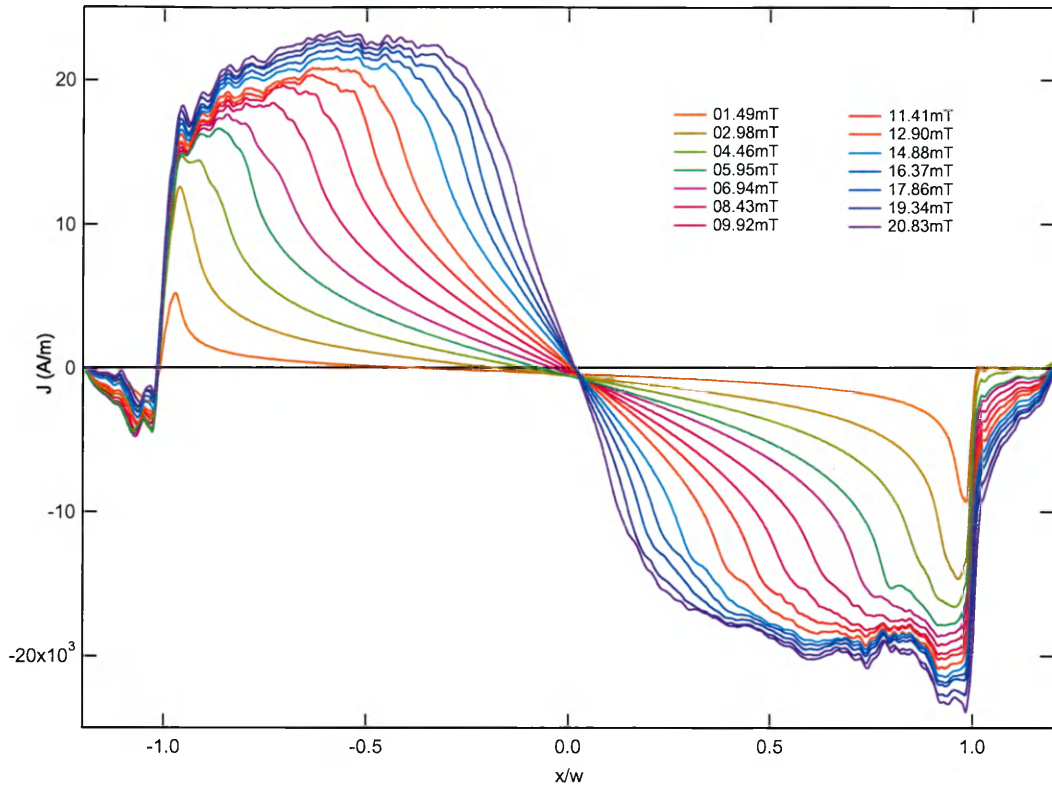


Fig. 28: Current density distribution calculated via inversion of the Biot-Savart law from the flux distribution. The asymmetry of the field profiles is reflected in the current distribution profiles.

To gain a deeper understanding of the sample response to a perpendicularly applied magnetic field the current distribution in the MgB_2 thin film is calculated from the magnetic field profiles via inversion of the Biot-Savart law (figure 28). Since the inversion procedure is based on a deconvolution transformation the result is affected by the limited region outside the sample. The effect of this limitation is particularly evident at the edges of the sample where a small current density $J \neq 0$, is calculated outside the boundary of the thin film. With respect to the left sample edge the current profiles show a steeper decrease to zero on the right side (figure 28). The current profiles for different values of the applied field are shown in figure 28. The asymmetry observed in the field distribution profiles is also reflected in the current distribution profiles shown in figure

28. According to the critical-state model a smooth plateau of equal height for all applied currents would have been expected on both sides of the sample, since J_c is assumed to be constant. However, the plateau height is dropping distinctly on both sides of the sample for $H_a < 7\text{mT}$. This effect is related to the rounding effect of the magneto-optical imaging technique which reduces the peak height. The appearance of the peak on the right side may be traced back to the very steep slope and the abrupt transition into a region with a less steep slope on the right side of the field profiles which becomes more pronounced for higher applied fields.

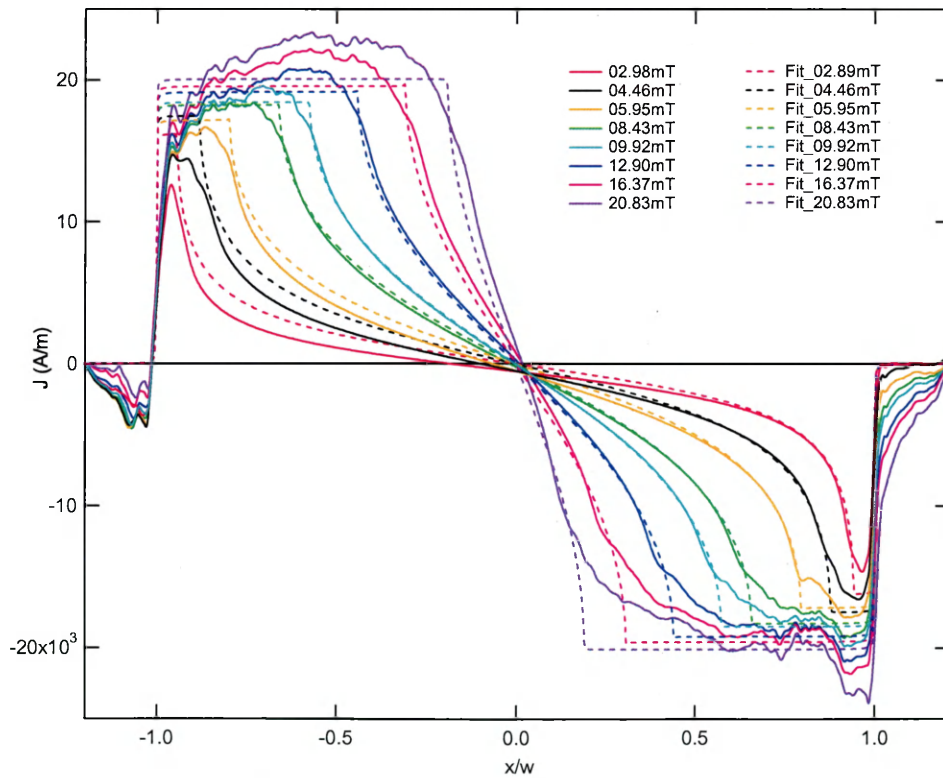


Fig. 29: The current profiles are fitted with eq. 10 from the critical-state model. Evident are the curvature on the left and the peak on the right side of the profiles.

The current profiles shown in figure 29 have been fitted with eq. 10. The fits overestimate the data on the right side towards the center, except at higher fields where the steep slope generates the peak.

According to ref. [23] the samples produced via reactive evaporation have a critical current density of $\sim 10^{10}$ A/m² at 36K. It has been shown, that the critical current density of high-temperature superconducting thin films increases as the temperature decreases. The effect is described by the following formula: [24, 25]

$$J_c(T) = J_{co} \left(1 - \frac{T}{T_c}\right)^n \quad (39)$$

J_{co} is the critical current density at $T = 0$ K, T_c is the critical temperature and $n = 1.6$ for YBCO. An increase by a factor of 14 at a temperature of 10K would be expected relative to $J_c(36K)$ for $n = 1$, or 68 for $n = 1.6$.

From the measurements an increase of J_c by a factor of 4 was determined with respect to J_c at 36K. A possible reason for the lower values is the sample cutting process, which involved exposing the sample to water. As previously stated MgB₂ is highly hygroscopic, and despite the tough magnesium- and boride - oxide surface layer the superconducting properties of the thin film might have been altered.

Both the magnetic field and current profiles were analyzed for different values of an external magnetic field applied perpendicular to the thin film surface. We found an overall good agreement of the averaged profiles with the critical-state model. Parts of the observed deviations are related to limits of the magneto-optical imaging technique or to

defects introduced by the processing procedure which could be improved. Some differences are more closely related to the material properties of MgB_2 that characterize the irregular finger-like flux structure observed in the magneto-optical images. This structure is not completely averaged out in the profiles and is responsible for the asymmetric flux penetration as well as the different growth behavior of the flux with respect to the edges. A more detailed two dimensional analysis that takes the irregularity of the flux front into account is attempted in section 4.2,.

4.1.2 Current Dependent Measurements

For the AC current dependent measurements an external magnetic field of about 10mT was applied to the sample after zero-field cooling to $T = 10\text{K}$. This way flux penetrates the sample and the effect of the current can be seen more clearly. The laser is triggered externally by the sinusoidal current applied to the sample, synchronizing the laser pulses with the desired phase point. Measurements are conducted for a transport current with a frequency of 400Hz at the maximum, minimum and zero - phase point. In this section the current dependent measurements will be studied. The phase dependent measurements can be found in the following section 4.1.3.

For a small applied AC current, which corresponds to only a few percent of the critical current, a strong effect on the flux distribution was observed. At 10K the critical current, as determined from prior measurements in section 4.1.1, is $I_c = 40\text{A}$. However, the maximum applied AC current is 0.5A before the magneto-optical image is lost, i. e., the superconducting state disappears.

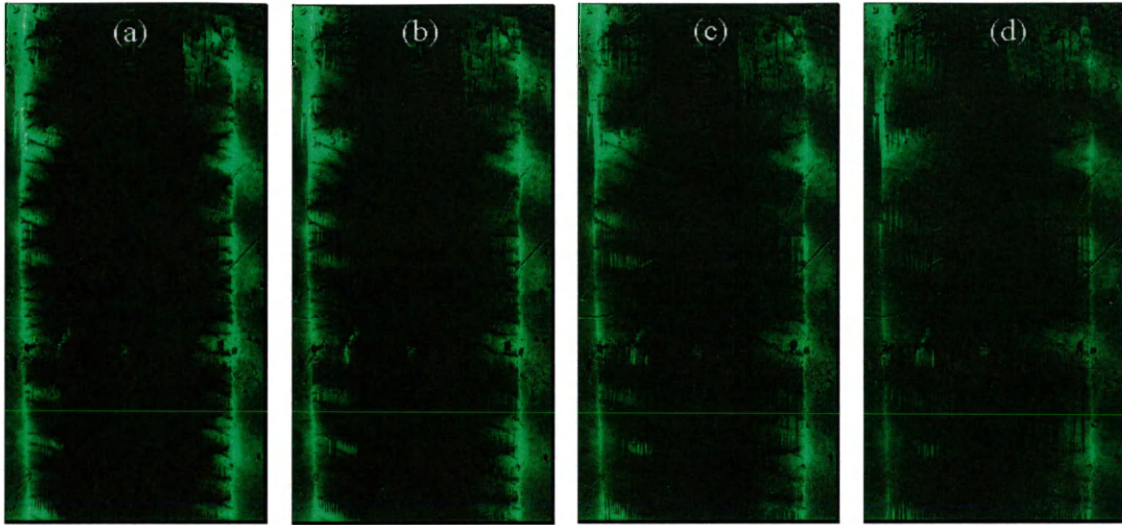


Fig. 30: The images show the effect of an increasing applied current from 0.337A (a), to 0.386A (b), 0.423A (c), and 0.473A (d). Clearly recognizable is the relaxation of the flux into the sample and the associated intensity decrease at the edges for increasing applied currents.

Figure 30 shows magneto-optical images for different values of the applied transport current. An increase in the transport current leads to a relaxation of the flux, which penetrates deeper into the sample. Additionally, the flux fingers become more blurry, since the flux density becomes redistributed in a broader area of the sample. The Lorentz force is responsible for the flux motion perpendicular to the direction of the applied transport current. When the Lorentz force is greater than the pinning force the flux lines move towards the center of the sample. According to the critical-state model this generally happens when the local value of the applied current is higher than J_c . However, heating the sample effectively lowers the pinning potential and reduces J_c which explains the observed flux relaxation. This effect will be investigated further later on, to attribute the observed flux relaxation to either the applied current or to Joule heating in the sample.

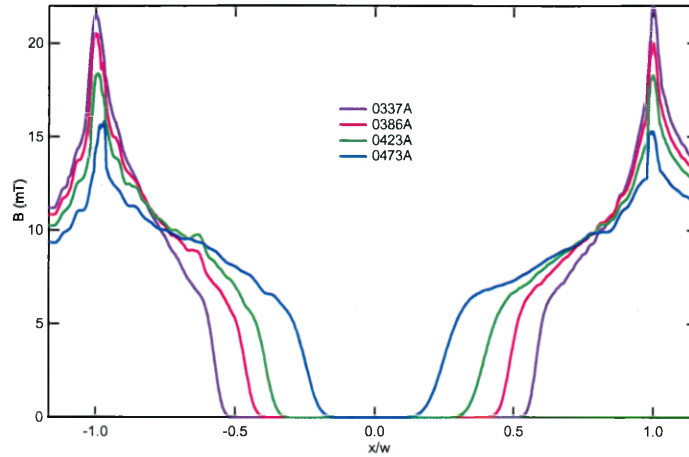


Fig. 31: The magnetic field profiles of the zero - phase point for different applied currents are depicted. For increasing currents the peak height reduces whereas the penetration depth of the flux increases.

The relaxation can be studied more quantitatively from the one-dimensional flux profiles. Figure 31 shows the flux profiles at the zero - phase points for different applied currents. The flux relaxes with higher currents, resulting in a decrease of the peak height while the penetration depth increases simultaneously. This confirms the strong effect of the applied AC current on the redistribution of the magnetic flux.

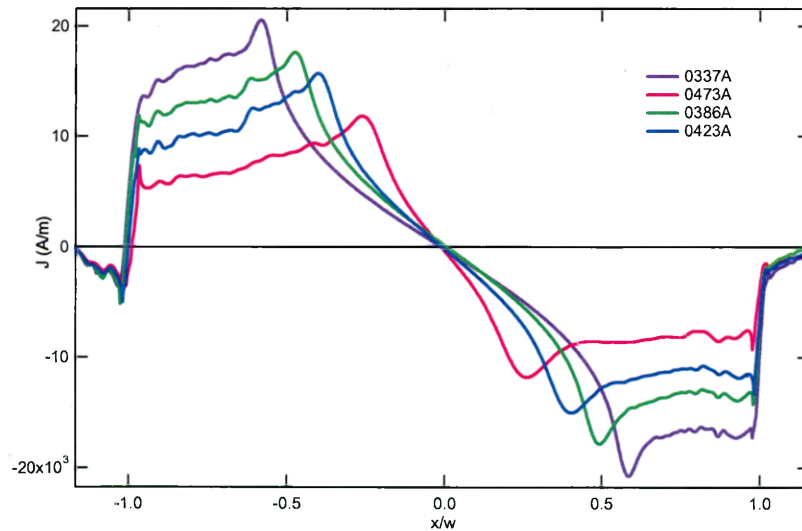


Fig. 32: The current profiles at the zero - phase point for different applied transport currents I_T are shown. With increasing transport current the plateau height is being reduced and the area where the current is flowing is getting wider.

Figure 32 shows the profiles for the zero - phase points for different transport currents. From the profiles it can be inferred that the area where the current is flowing becomes wider as the plateau width increases.

The plateaus are not flat and smooth but display prominent peaks towards the sample center. This is in accordance with the shape of the flux profiles depicted in figure 31, which display some sort of plateau in the relevant area before dropping drastically towards the field free region. The different behavior, with respect to the field-dependent measurements, can be explained by the different manner in which the flux penetrates the thin film, i. e. driven by the applied magnetic field or by the relaxation effect of the applied current, respectively.

Instead of the constant plateau height predicted by the critical-state model we observe a decrease in J_c for higher applied currents. To determine the origin the corresponding temperature increase is calculated with eq. 39 (sec. 4.1.1), assuming $n = 1$. The temperature variation is calculated with the heat capacity equation $dQ = C dT$, where $C = 70\text{mJ/K}$ is the heat capacity for MgB_2 and dQ is the heat added to the power dissipated by the contacts for the different applied currents. The power was calculated with the Joule law $P = I^2 R$.

The results, listed in table 1, indicate that the loss of the signal is most probably due to heating by the contact resistance and not the AC current itself. The heat generated in the thin film was high enough to briefly increase the temperature to approximately 38K leading to the loss of the signal at small transport currents. Hence the decrease in plateau height can be explained: The pinning ability of the sample is reduced by the strong

heating which effectively lowers the pinning potential of the defect sites despite continuous cooling with helium. Additionally, the relaxation of the flux must partially be attributed to the strong heating effect instead to an effect of the AC current itself. In order to avoid increasing the temperature of the thin film in the future the contacts have to be improved.

| I_T / A | Power / Watt | Heat / J | $\Delta T / \text{K}$ |
|------------------|--------------|----------|-----------------------|
| 0.337 | 0.30 | 0.41 | 5.80 |
| 0.386 | 0.39 | 0.78 | 11.13 |
| 0.423 | 0.51 | 1.10 | 15.26 |
| 0.473 | 0.66 | 1.50 | 21.42 |

Table 1: The table shows the values for the dissipated power, the generated heat and the increase in temperature.

The effect of a small transport current on the flux evolution in the MgB_2 thin film was analyzed as a function of the applied transport current. The strong relaxation effect was found to be related to the heat generated at the contact resistance of the sample. Differences in the development of the flux, with respect to the field-dependent measurements, can be attributed to the different driving forces.

4.1.3 Phase Dependent Measurements

In this section the flux development for different transport currents will be discussed with respect to the phase of the applied current. For the phase dependent measurements magneto-optical images were taken at the *min*, *max* and zero - phase point of the sinusoidal transport current. Because of the small applied current only a small intensity

shift is visible at the sample edges indicating the effect of the different current phase points. A quantitative analysis is performed on the one-dimensional cross section profiles.

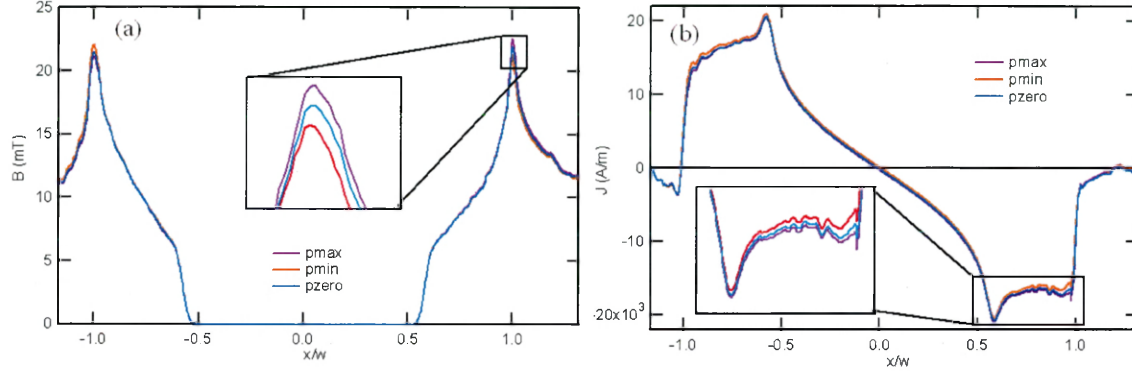


Fig. 33: Field (a) and current (b) distribution for an applied current of $I_T = 0.337\text{A}$. The insets show the effect of the different phase point profiles for the field and current distribution respectively.

The field profiles of the three phase points in figure 33 (a) show a good overlap in the thin film. The applied current adds to the shielding current on one side but reduces the magnitude on the other. Both peaks have about the same total height. No transport current is flowing at the zero-phase point, and its profile lies in between the *max* and *min* profiles. A 4.5 to 7.5% difference in peak height of the field profiles is observed.

The current profiles shown in figure 33 (b) were calculated from the field profiles via inversion of the Biot-Savart law. They also overlap very well in the central region. Closer to the edge the current profiles can be distinguished clearly from one another which reflects the effect of the phase on the field profiles.

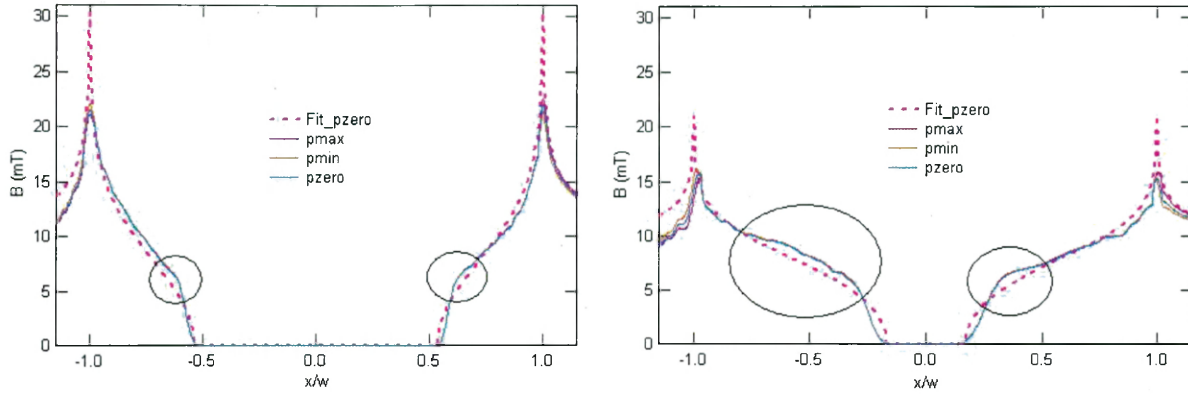


Fig. 34: The left and right panel shows the flux distribution for a transport current $I_T = 0.337\text{A}$ and $I_T = 0.473\text{A}$, respectively. Dotted lines are fits eq. 14. The dark circles mark deviations

Figure 34 shows the field profiles for the lowest (left panel) and highest applied current (right panel). The general flux distribution in the MgB_2 sample is reproduced well by fits of eq. 14, although of the critical-state model does not consider a transport current.

The overall agreement with the critical-state model is better for lower applied currents. The two ‘bumps’ (see dark circles in figure 34) on either side of the profiles grow more pronounced for higher currents as shown in figure 34. As observed in sect. 4.1.2 the initial heating leads to flux relaxation and the formation of ‘plateaus’ in the profiles stretching towards the sample center. Close to the field free region the profiles then drop to zero with a rather steep slope, which can be attributed to the cutting and smoothing procedure. The general deviation from the critical-state model, however, originates in the irregular finger-like structure of the flux and the way the flux penetrates the sample according to the driving force. The distinct behavior of the flux front in both field and current dependent measurements is discussed in section 4.2.

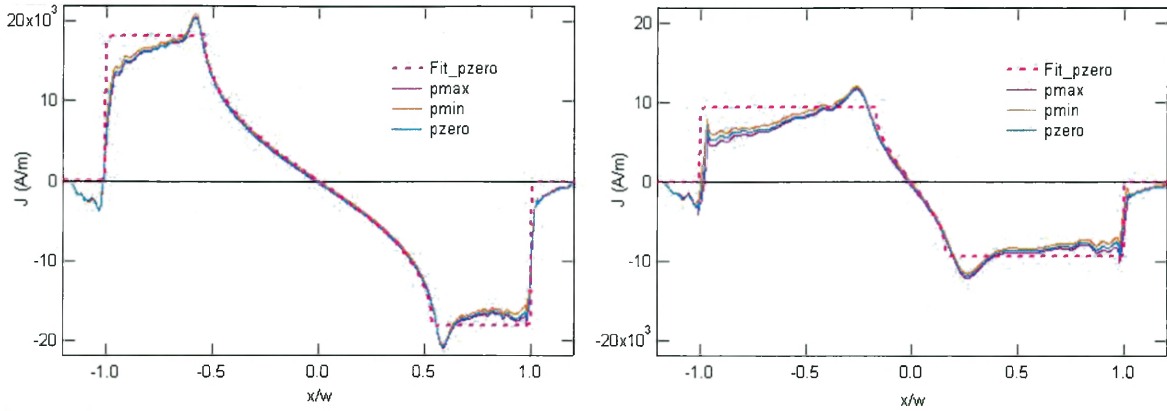


Fig. 35: The left and right panel shows the current profiles for a transport current of 0.337A and 0.473A respectively. The dotted lines are the critical-state model fits, eq. 10.

The current distribution shown in figure 35 has been calculated from the magnetic field profiles by inverting the Biot-Savart law. The appearance of the peaks in the central region deviates from the expected constant plateau height and coincides with the particularly steep drop of the field profiles (figure 34), discussed previously. The general agreement of the profiles with the critical-state model is good for all applied currents.

For the phase dependent measurements we find that the field and current profiles can be fitted with the critical-state model in the case of small applied currents. Deviations are attributed to the distinct flux penetration. The small phase effect observed in the field and current profiles agrees with the theory. It is particularly distinct at the edges of the sample and grows more pronounced for higher currents, which is in accordance with theory and is underlined by the transport current profiles discussed in section 4.1.4.

4.1.4 Transport Current Analysis

From the one-dimensional total current distribution profiles the transport current I_T is calculated by eliminating the shielding current flowing in the thin film. This is achieved by subtracting the zero - phase point profile from the max. and min. phase point profiles. [26] The resulting transport current profiles are shown in figure 36. The red curves represent the transport current at the minimum phase point, and the blue curves at the maximum phase point. The sign of the current is different since the applied transport current is flowing in opposite directions at the two phase points.

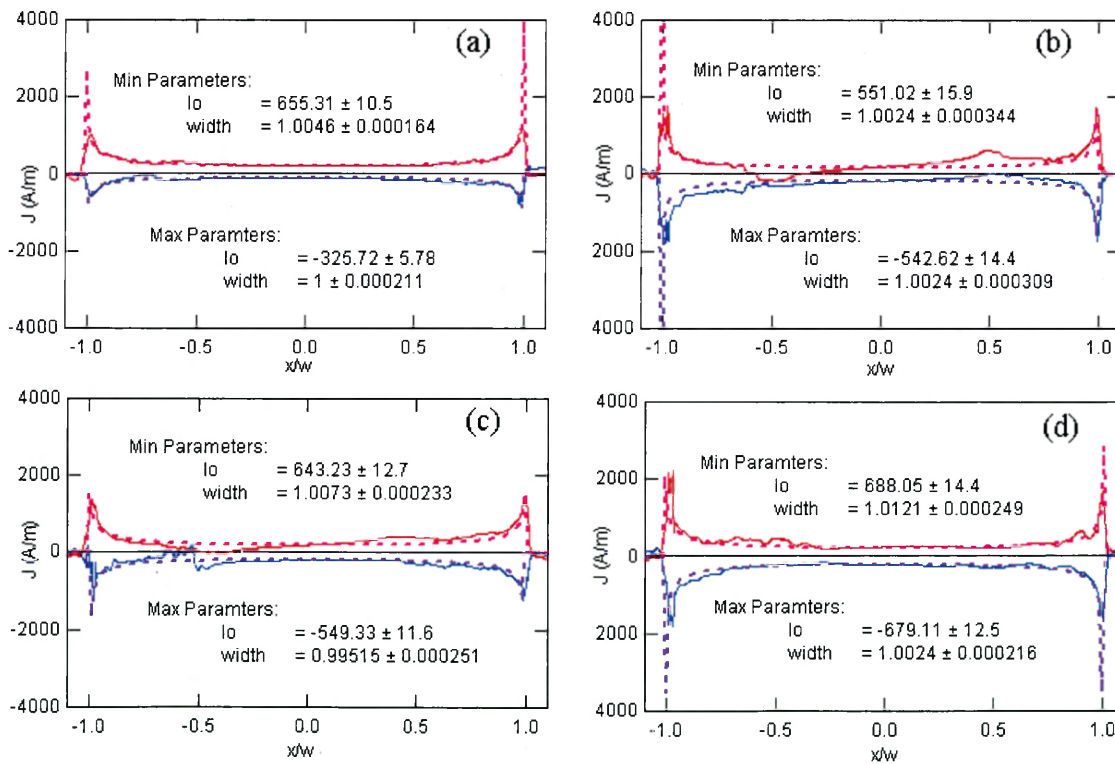


Fig. 36: The graphs show the transport current profiles for different applied currents 0.337A (a), 0.386A (b), 0.423A (c) and 0.473A (d). The red and the blue curves represent the transport current obtained by subtracting the zero - phase point from the min. and max. phase point of the total current profiles, respectively. The data was fitted with eq. 18. Fits are represented by the dotted lines.

According to theory the transport current is flowing in the whole sample but displays distinct peaks at the edges. The profiles have been fitted with eq. 18, which represents the theoretical distribution of a transport current applied to a superconducting thin film. Figure 36 shows that the fits agree very well with the data. The irregular flux penetration as well as the processing of the data in the central region may have influenced the line profiles. Despite the small magnitude of the transport current, which contributes only 2% to the total current in each half of the flux, the profiles can be obtained.

A quantitative check is done by calculating the transport current I_T from the profiles. The original profiles are integrated over the width of the thin film yielding the transport current I_T that flows in the sample at the two different phase points. Since for the different phase points the amplitude of the transport current only changes sign, the integrated values for the min. and max. phase point should be equal. The average transport current values of the two phase points are shown in table 2 as well as the deviations from the applied currents. For $I_T = 0.386\text{A}$, a major deviation is observed due to the large ‘negative current’ (see figure 36 (b)) that reduces the integrated value greatly.

Another method to extract the magnitude of the transport current is to fit the profiles with eq. 18 and to calculate I_T from the fitting parameter I_o . This yields a very good agreement with the applied transport current. The values are also shown in table 2.

| I_T / A | Integrated I_T / A | Accuracy / % | Fitted I_T / A | Accuracy / % |
|-----------|----------------------|--------------|------------------|--------------|
| 0.337 | 0.334 | 2 | 0.347 | 3 |
| 0.386 | 0.371 | 4 | 0.387 | 1 |
| 0.423 | 0.292 | 31 | 0.435 | 1 |
| 0.473 | 0.5 | 7 | 0.483 | 2 |

Table 2: Comparison of the transport current values calculated via integration of the transport current profiles and via fitting of the transport current profiles.

Both calculations show that the transport current can be calculated accurately from the current profiles, demonstrating that the time-resolved magneto-optical imaging technique is sensitive to very small changes in the flux distribution induced by the applied current.

Figure 37 compares the rescaled total current profiles and the transport current profiles for the lowest and the highest applied current. The grey areas mark where 90% of the applied current is effectively flowing in the thin film. It covers $\sim 85\%$ of the sample for the lowest current, and $\sim 88\%$ for the highest current. Hence the transport current is not flowing uniformly in the sample, but with an emphasis on the edges as indicated by the transport current profiles in figure 36.

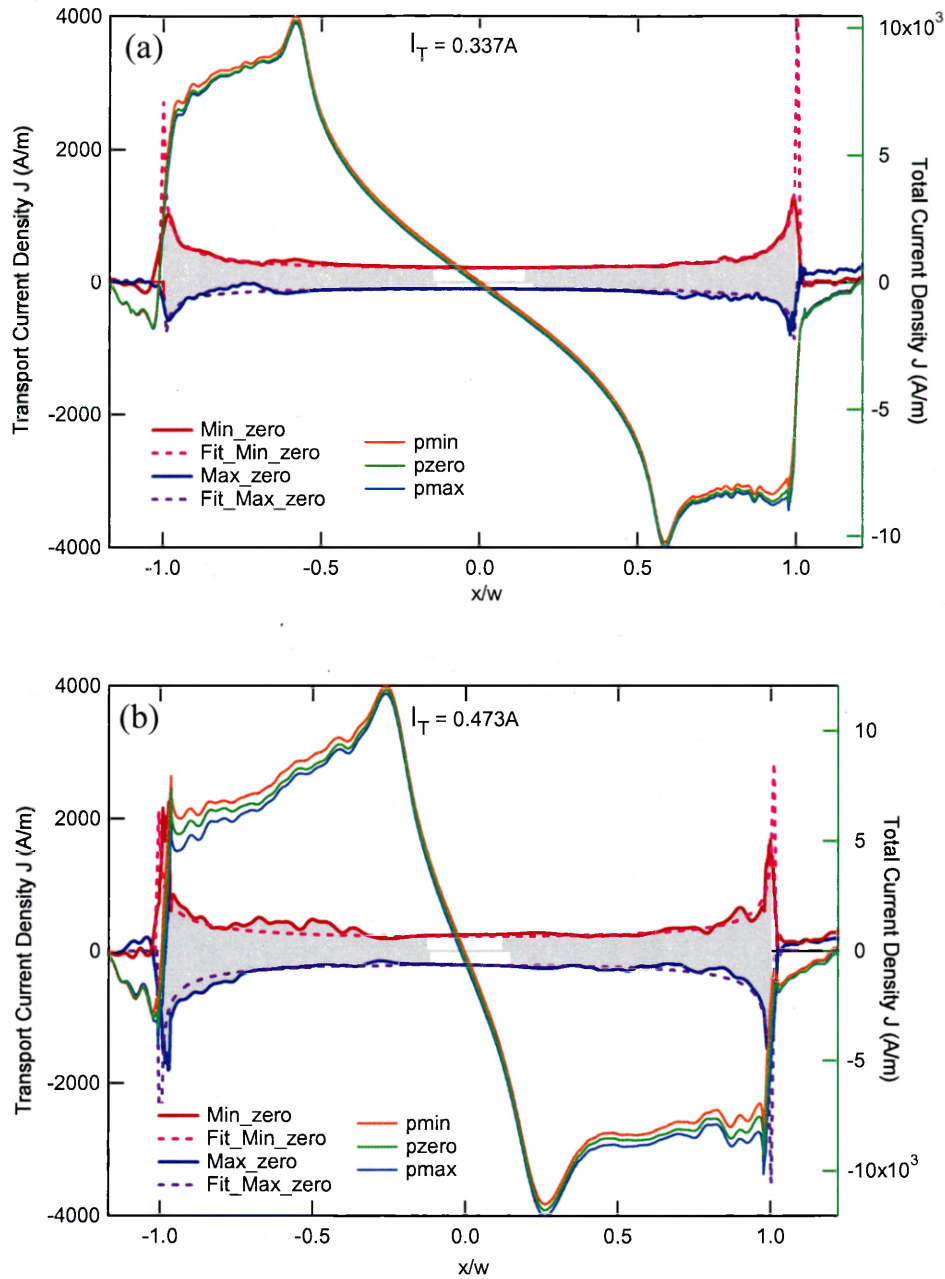


Fig. 37: The red and blue curves represent the transport current profiles obtained by subtracting the zero - phase point of the total current density of the min. and the max phase point, respectively. Comparing the total current density, dominated by the shielding current, with the transport current density one notices that the fanning out effect is occurring distinctly where the transport current is flowing. The grey area indicates where 90% of the applied current is flowing in the sample. For the higher transport current (b) the peak of the transport current profiles increases in height with respect to the lower current (a). The total current density in (a) has been rescaled by a factor of 0.5 for better comparison.

4.2 Statistical Analysis

Previously the analysis was limited to averaged one-dimensional profiles where the irregular penetration and the inhomogeneous flux front were not considered. By studying the growth of the flux front in MgB₂ an understanding of the flux penetration can be obtained with respect to the intrinsic properties of MgB₂, as well as the effect of a dynamic driving force added by applying a transport current. The procedure with which the flux front contour and finally the power law exponents were determined is described in appendix A.

The interest of this study lies in the relation of the scaling exponents to the origin of the roughening: the pinning sites. They are present also in clean films due to defects in the molecular structure of the grown films. The pinning leads to a roughening of the flux front. Thus different roughness exponents for static or dynamic measurements may hint towards a different pinning strength in the various thin film superconductors giving information about the pinning landscape. [27]

4.2.1 Static Measurements

The roughness of the flux front penetrating into the MgB₂ thin film is studied with eq. 26. $C(l)$ is calculated for the flux front profiles and fitted with eq.

$$y(l) = y_0 + A \cdot l^\alpha . \quad (40)$$

in order to determine the scaling exponent α as a function of the applied field.

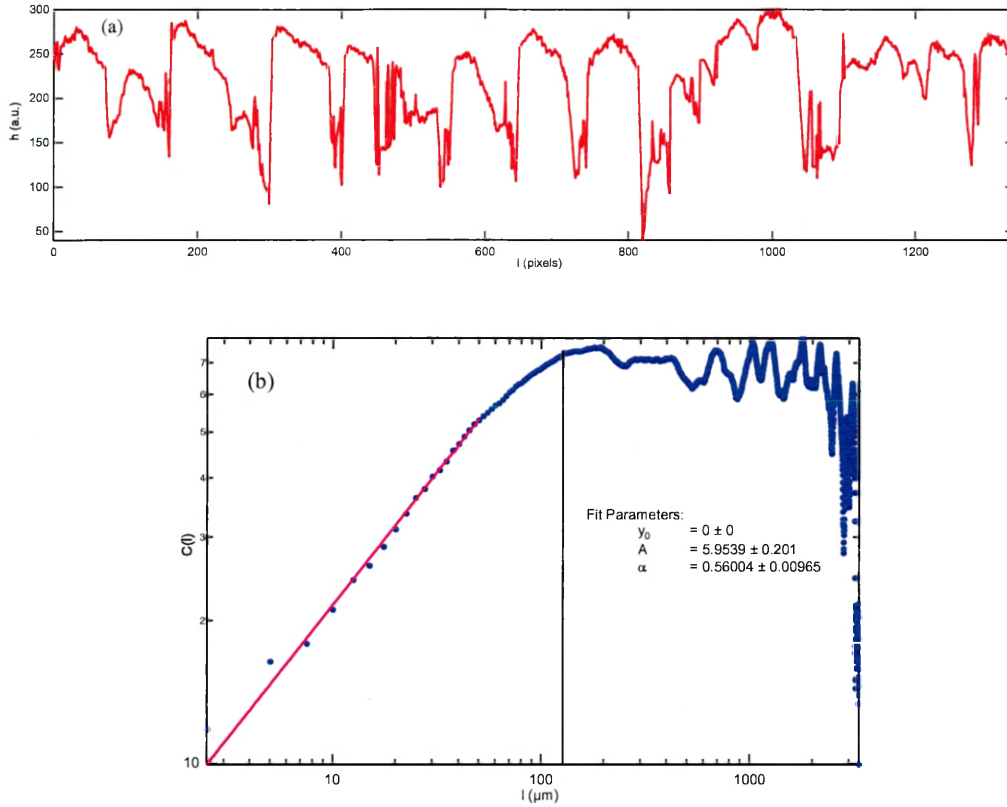


Fig. 38: The interface from which $C(l)$ was calculated (a) and the associated double logarithmic plot of $C(l)$ over l (b) are shown. The black line indicates the value l_{sat} at which the function goes into saturation. The function was fitted with the power law eq. 40. The data was extracted from the flux front of the upper edge at an external applied magnetic field of 20.83mT. The purple line is the fit with eq. 40.

Figure 38 (a) shows an example of a flux front profile extracted from the images as described in appendix A and the corresponding double logarithmic plot of the two point correlation function $C(l)$ as a function of the separation l between two points (b).

$C(l)$ shows a strong power law behavior that goes into saturation at a characteristic value of l_{sat} . This value corresponds to the average width of the finger patterns as indicated by the black lines of length l_{sat} at the saturation point shown in figure 38 (b).

The slope of the graph in figure 38 (b) indicates that the changes in $C(l)$ between two points separated by l is changing greatly. The formation of the plateau suggests that

at a certain value of l the variations in $C(l)$ are less dramatic than for smaller values and stay essentially equal. For higher values, however, noise appears around the still visible plateau since the average of $[h(x+l) - h(x)]^2$ can not be calculated for as many values as for smaller l due to the limited system size.

The average value of all exponents extracted from the field-dependent measurements was calculated to be $\alpha = 0.58 \pm 0.09$. The numerically calculated value from the DPD model is 0.63, which is a little higher than the one obtained experimentally but lies within the estimated error of 15%. The result places the static flux front growth of MgB₂ in the same class as the interface growth of YBCO and Nb. Deviations from the expected values may sometimes be attributed to low contrast in the images and in parts to the difficulty to recognize the exact course of the flux front. The processing of the data, described in appendix A, may also add to the deviations and may be improved.

4.2.2 Dynamic Measurements

The directed percolation depinning model can also be applied to dynamic systems and uses the same scaling exponents. The applied transport current I_T can be considered as a dynamic driving force behind the flux motion. The zero - phase point of the AC current is studied only. The AC current is flowing continuously and hence the Lorentz force F_p is permanently acting on the flux lines. This means that the vortex distribution is constantly altered as is the critical probability p_c which is related to the pinning force and responsible for the flux front growth to stop or continue. The two point correlation function $C(l)$ is plotted as a function of l in a double logarithmic scale as shown in figure 39 and fitted with eq. 40.

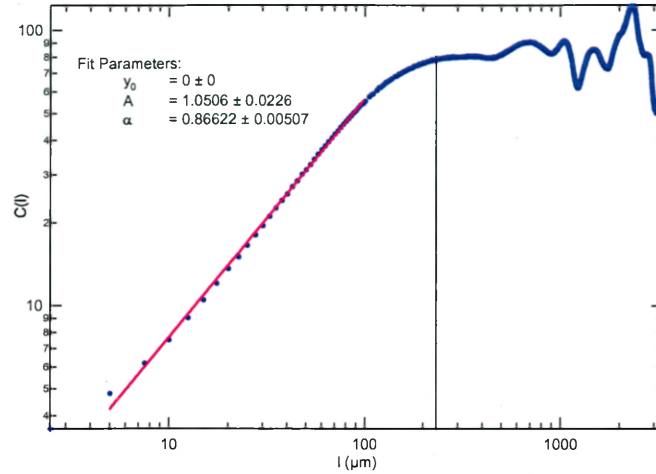


Fig. 39: Double logarithmic plot of $C(l)$ over l . The data was extracted from the zero - phase point image with a transport current of 0.423A and fitted with eq. 40. The graph shows the same distinct behavior as for the field-dependent measurements. The fit is purple, while the data points are blue.

The average exponent value for the dynamic measurements is calculated to be $\alpha = 0.78 \pm 0.12$, which is close to $\alpha \approx 0.7$, obtained by the DPD model [21]. According to ref. [20] the experimentally obtained exponents may be higher than numerically calculated ones because of the long range repulsion forces between the vortices.

Compared to the static measurements the dynamic measurements show a distinct increase in the exponent value, which is consistent with the prediction of the DPD model. This shows that the driving forces behind the flux motion are different as was already reflected in the averaged profiles for field and current dependent measurements. Hence static and dynamic driving forces influence the flux front growth notably different although the flux front may look identical or similar at first glance.

This represents the first self organized criticality study on superconducting MgB_2 thin films.

5 Conclusions

A superconducting MgB₂ thin film has been studied with the time-resolved magneto-optical imaging technique and analyzed in terms of the critical-state model.

The field-dependent measurements show an overall good agreement with the critical-state model. The irregular finger-like structure of the penetrating flux gives rise to slightly asymmetric field and current profiles. Relaxation effects caused by a small transport current applied to the sample were attributed to heat generated at the contact resistance. The transport current profiles are in good agreement with the theory and show that the applied current is not flowing uniformly in the sample but is higher at the edges.

The irregular flux evolution is analyzed with a statistical method based on the scaling laws of interface growth. Concerning both static and dynamic measurements, distinct exponents were determined indicating different driving forces. The results are consistent with the directed percolation depinning model, placing MgB₂ in the same universality class as YBCO and Nb. This may hint towards a common underlying mechanism influencing the flux evolution in those three profoundly different high-temperature superconductors.

6 Appendix – Interface Growth

The flux front in the magneto-optical images is analyzed with the two point correlation function $C(l)$ from eq. 26. In order to calculate $C(l)$ the most adequate intensity value corresponding to the flux front was traced as shown in figure 40. It was equal for all analyzed images in order to obtain comparable results.

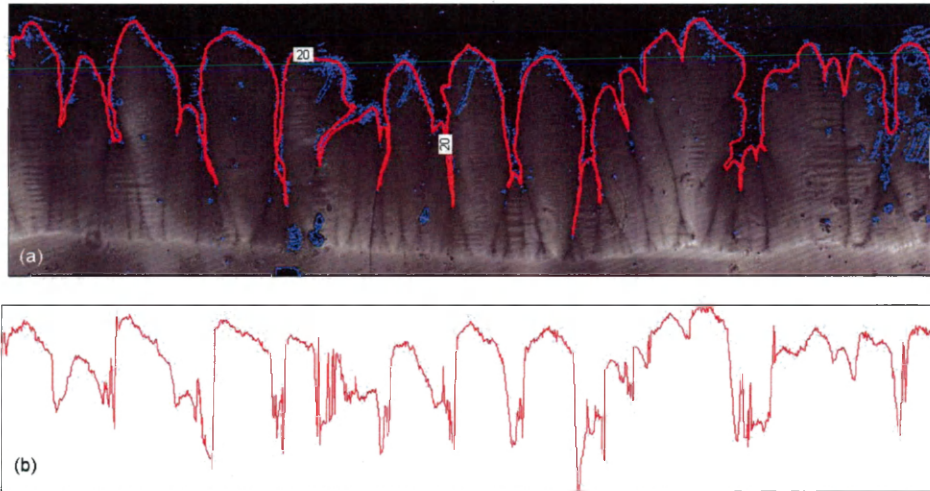


Fig. 40: (a) Upper edge of the original image for an applied field of 20.83mT with contour plot corresponding to a magnetic field value of ~ 7 mT. (b) Result after averaging and excluding irrelevant data

Figure 40 shows that the chosen intensity value does not exclusively correspond to the flux front. In order to extract the profile of the interface the relevant contour was traced by hand. To include the most relevant information about the flux front one averaged over an interval of about 10 to 15 pixels around the red hand drawn line depicted in figure 40 (a). The result can be seen in figure 40 (b).

In order to remove eventual influence of the rough sample edges, the edge profiles are subtracted from the flux front profiles. Afterwards the two point correlation function $C(l)$ was calculated.

Figure 41 shows a plot which is to be expected from a self-affine interface. The plots show a strong power law behavior for small values of l and go into saturation at a value l_{sat} . By fitting the graph with eq. 40 the exponent α that characterizes the roughness of the system is obtained.

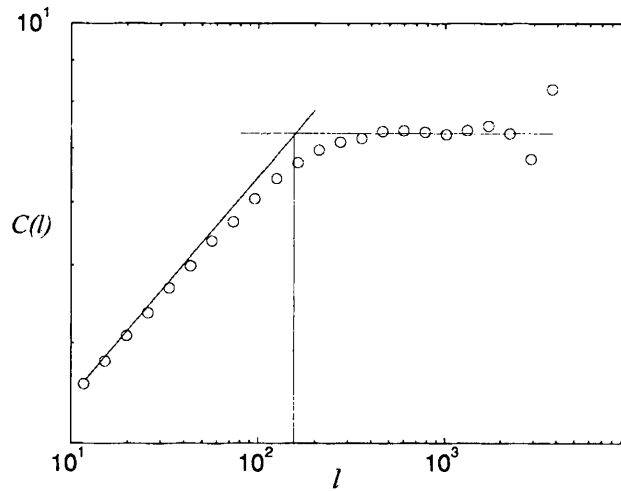


Fig. 41: Expected plot for the two point correlation function $C(l)$ as a function of l for a self affine interface. [21]

7 References

- [1] A. P. Malozemoff, J. Maguire, b. Gamble, S. Kalsi; Power Applications of High-Temperature Superconductors: Status and Perspectives; Applied superconductivity, Vol. 12, No. 1, (2002)
- [2] J. Nagamatsu, N. Nakagawa, T. Muranaka, Y. Zenitani, J. Akimitsu; Superconductivity at 39 K in magnesium diboride, Nature, Vol. 410, No. 1 (2001)
- [3] H. J. Choi, D. Roundy, H. Sun, M. L. Cohen, S. G. Louie; The origin of the anomalous superconducting properties of MgB₂; Nature ,Vol 418, 15 (2002)
- [4] Y. Bugoslavsky, G. K. Perkins, X. Qi, L. F. Cohen, A. D. Caplin; Vortex dynamics in superconducting MgB₂ and prospects for applications; Nature Vol. 410, No. 29, (2001)
- [5] T. H. Johansen, M. Baziljevich, D. H. Shantsev, P. E. Goa, Y. M. Galperin, W. N. Kang, H. J. Kim, E. M. Choi, M. -S. Kim, S. I. Lee; Dendritic magnetic instability in superconducting MgB₂ films; Europhys. Lett., 59 (4), pp. 599-605 (2002)
- [6] A. L. Rakhmanov, D. V. Shantsev, Y. M. Galperin, T. H. Johansen; Finger patterns produced by thermomagnetic instability in superconductors; Phys. Rev. B 70, 224502 (2004)
- [7] D.V. Denisov, D.V. Shantsev, Y. M. Galperin, Eun-Mi Choi, Hyun-Sook Lee, Sung-Ik Lee, A.V. Bobyl, P. E. Goa, A. A. F. Olsen, and T. H. Johansen; Onset of Dendritic Flux Avalanches in Superconducting Films; Phys. Rev. Let. 97, 077002 (2006)
- [8] D. V. Denisov, A. L. Rakhmanov, D. V. Shantsev, Y. M. Galperin, T. H. Johansen; Dendritic and uniform flux jumps in superconducting films; Phys. Rev. B 73, 014512, (2006)
- [9] I. S. Aranson, A. Gurevich, M. S. Welling, R. J. Wijngaarden, V. K. Vlasko-Vlasov, V. M. Vinokur, U. Welp; Dendritic Flux Avalanches and Nonlocal Electrodynamics in Thin Superconducting Films; Phys. Rev. Let. 94, 037002, (2005)
- [10] F. L. Barkov, D. V. Shantsev, T. H. Johansen, P. E. Goa, W. N. Kang, H. J. Kim, E. M. Choi, S. I. Lee; Local threshold field for dendritic instability in superconducting MgB₂ films; Phys. Rev. B 67, 064513 (2003)
- [11] C. Buzea, T. Yamashita; Review of the superconducting propterties of MgB₂; Supercond. Sci. Technol. Vol. 14, (2001) R115 – R146

- [12] Y. Cui, J. E. Jones, A. Beckley, R. Donovan, D. Lishego, E. Maertz, A. V. Pogrebnyakov, P. Orgiani, J. M. Redwing, X. X. Xi; Degradation of MgB₂ Thin Films in Water; *Applied Superconductivity*, Vol. 15, No. 2 (2005)
- [13] M. Iavarone, G. Karapetrov, A. E. Koshelev, W. K. Kwok, G. W. Crabtree, D.G. Hinks, W. N. Kang, E.-M. Choi, H. J. Kim, H.-J. Kim, S. I. Lee; Two-Band Superconductivity in MgB₂; *Phys. Rev. Let.*, Vol. 89, No. 18
- [14] S. Souma, Y. Machida, T. Sato, T. Takahashi, H. Matsui, S.-C. Wang, H. Ding, A. Kaminskik, J. C. Campuzanok, S. Sasaki, K. Kadowaki; The origin of multiple superconducting gaps in MgB₂, *Nature*, Vol. 423, No. 1 (2003)
- [15] Ch. Jooss, J. Albrecht, H. Kuhn, S. Leonhardt, H. Kronmüller; Magneto-optical studies of current distributions in high-*T_c* superconductors; *Rep. Prog. Phys.* 65, 651–788 (2002)
- [16] C. P. Bean; Magnetization of Hard Superconductors; *Phys. Rev. Let.* Vol. 8, No. 6, (1962)
- [17] E. Zeldov, J. R. Clem, M. McElfresh, M. Darwin; Magnetization and transport currents in thin superconducting films; *Phys. Rev. B* Vol. 49, No. 14, (1994)
- [18] M. E. Gaevski, A. V. Bobyl, D. V. Shantsev, A. F. Ioffe, Y. M. Galperin, T. H. Johansen, M. Baziljevich, H. Bratsberg, S. F. Karmanenko; Magneto-optical study of magnetic-flux penetration into a current-carrying high-temperature-superconductor strip; *Phys. Rev. B*, Vol. 59, No. 14, (1999)
- [19] P. Bak, C. Tang, K. Wiesenfeld; Self-organized criticality; *Phys. Rev. A* Vol. 38, No. 1, (1988)
- [20] V. K. Vlasko-Vlasov, U. Welp, V. Metlushko, G. W. Crabtree; Experimental test of the self-organized criticality of vortices in superconductors; *Phys. Rev. B* 69, 140504(R) (2004)
- [21] A. -L. Barabási, H. E. Stanley; *Fractal Concepts in Surface Growth*; Cambridge University Press, (1995)
- [22] Z. Ye, Q. Li, W. D. Si, M. Suenaga, V. F. Solovyo, P. D. Johnson; Response of fractal penetration of magnetic flux to disorder landscape in superconducting films; *Phys. Rev. B* 72, 134514, (2005)
- [23] B. H. Moeckly, W. S. Ruby; Growth of high-quality large-area MgB₂ thin films by reactive evaporation; *Supercond. Sci. Technol.* Vol. 19 (2006), L21–L24

- [24] A.A. R. Fernandes, I. N. Chan, J. Guimpel, O. Nakamura, D. Lederman, I. K. Schuller; Scaling of critical currents in high-temperature superconducting superlattices and thin films; Appl. Phys. Lett. 61, 3181 (1992)
- [25] Y. Yeshurun, A. P. Malozemoff; Giant Flux Creep and Irreversibility in an Y-Ba_Cu_O Crystal: An Alternative to the Superconducting-Glass Model; Phys. Rev. Lett. Vol. 60, No. 21, (1988)
- [26] Lucarelli et al. – Submitted to APL
- [27] R. Surdeanu, R. J. Wijngaarden, E. Visser, J. M. Huijbregtse, J. H. Rector, B. Dam, R. Griessen; Kinetic Roughening of Penetrating Flux Fronts in High- T_c Thin Film Superconductors; Phys. Rev. Lett. Vol 83, No. 10 (1999)
- [28] A. Lucarelli, G. Lüpke, T. J. Haugan, G. A. Levin, P. N. Barnes; Time-resolved magneto-optical imaging of Y1Ba2Cu3O7- δ thin films in high-frequency AC current regime; Superconductor Science and Technology Vol. 19, (2006), 667-670
- [29] A. Frey; Time-Resolved Magneto-Optical Imaging of Superconducting YBCO Thin Films in the High-Frequency AC Current Regime; Master Thesis, College of William & Mary, July 2006